Contributions to Mineralogy and Petrology (2025) 180:26
https://doi.org/10.1007/s00410-025-02213-9

ORIGINAL PAPER

Plagioclase crystal size distributions, growth and nucleation rates in an anhydrous arc basaltic andesite

Melvyn Billon[1] · Jacqueline Vander Auwera[1] · Olivier Namur[2] · François Faure[3] · Marian Barbara Holness[4] · Bernard Charlier[1]

Received: 9 December 2024 / Accepted: 28 February 2025

Abstract

We experimentally investigated plagioclase nucleation and growth in anhydrous arc basaltic andesite at 1 atm and Ni-NiO equilibrium. After equilibration at 1190 °C (15 °C above the liquidus) for 24 h, experiments were cooled at 1, 3, or 9 °C/h and quenched at 1175–1000 °C. New plagioclase grains nucleated near the liquidus, followed by minor amounts of Fe–Ti oxides and pyroxene below 1120 and 1050 °C, respectively. Plagioclase shapes varied from 2D tabular/elongated (1 and 3 °C/h) to hopper and swallowtail textures (9 °C/h), suggesting a transition from interface- to diffusion-controlled growth. Crystal shapes and sizes were correlated, with the smallest and largest having equant/elongated and tabular/bladed 3D shapes, respectively. To identify the most suitable method for inferring storage timescales in natural magmas, we calculated nucleation (J) and growth rates (G) with different methods: G_{max} from the average size of the 10 biggest crystals, G_{mean} from the entire crystal population, J_{batch} and G_{batch} from the number and proportion of plagioclase estimated by point counting, and J_{CSD} and G_{CSD} from the crystal size distribution (CSD). J and G were greatest near the liquidus and decreased during cooling; the decrease was minimal at slow cooling rates, making G nearly constant. G decreased with decreasing cooling rates (from 10^{-7} to 10^{-9} cm/s at 9 and 1 °C/h, respectively), stabilizing after ~ 20 h of cooling. These variations of G principally resulted from differences in experimental conditions, more than the calculation method considered. Given the uncertainties of CSD theory in closed systems and the size and crystallographic axis-dependence of growth rates, combining G_{mean} and G_{max} appears to be the most effective method for experimentally determining growth rates. However, the batch method (J_{Batch}) still provides a good estimate of J.

Keywords Cooling rate · Texture · Aspect ratio · 3D shape

Introduction

Magma solidification occurs via crystal nucleation and growth (e.g. Cashman 1990) and is recorded as chemical and/or textural changes within crystals. Crystallization timescales are crucial when assessing pre-eruptive dynamics, including magma storage (Cooper and Kent 2014) and ascent dynamics (Humphreys et al. 2008; Rutherford 2008; Armienti et al. 1994, 2013). Timescales have been estimated using techniques such as uranium-series disequilibria (Cooper and Kent 2014), diffusion relaxation in crystals (Costa et al. 2008), and, most commonly, crystal size distributions (CSDs; Cashman 1993; Kent et al. 2010). This latter approach is particularly useful in the absence of secondary phases used for dating. However, it requires knowledge of crystal growth rates to convert crystal sizes to time.

Communicated by Hans Keppler.

✉ Melvyn Billon
melvyn.billon@uliege.be; melbillon@gmail.com

[1] Département de Géologie, Université de Liège, Allée du Six-Août 12, 4000 Liège, Belgium

[2] Department of Earth and Environmental Sciences, KU Leuven, Celestijnenlaan 200E, 3001 Louvain, Belgium

[3] Université de Lorraine, CNRS, CRPG, UMR 7358, 15 Rue Notre Dame Des Pauvres, 54501 Vandoeuvre-lès-Nancy, France

[4] Department of Earth Sciences, University of Cambridge, Downing Street, Cambridge CB2 3EQ, UK

Published online: 19 March 2025

In many volcanic rocks, plagioclase is the most abundant crystal phase and commonly records magmatic conditions (T, P, melt H_2O content) because of the slow coupled CaAl-NaSi diffusion (Grove and Baker 1984; Morse 2013; Bennett et al. 2019). Plagioclase crystal habits reflect crystallization kinetics as well as changes of temperature, pressure, and composition (i.e. magma mixing) (Couch et al. 2001, 2003a; b; Hammer and Rutherford 2002; Del Gaudio et al. 2010; Cassidy et al. 2016; Bennett et al. 2019).

Basaltic andesites and andesites are very common arc magma compositions (Reubi and Blundy 2009; Kent et al. 2010). However, most experimental determinations of plagioclase growth rates have been performed on basaltic compositions (e.g. Kirkpatrick 1977; Cashman 1993; Lesher et al. 1999; Pupier et al. 2008), with only a few studies devoted to andesites (Shea and Hammer 2013; Vetere et al. 2021) or dacites (Hammer and Rutherford 2002; Brugger and Hammer 2010a, b). Available results range from 10^{-9} to 10^{-6} cm/s in basalts (e.g. Lesher et al. 1999; Orlando et al. 2008; Giuliani et al. 2020) to 10^{-8}–10^{-7} cm/s in andesites (Shea and Hammer 2013; Vetere et al. 2021) and 10^{-11}–10^{-8} cm/s in dacites (Hammer et al. 1999; Hammer and Rutherford 2002; Brugger and Hammer 2010a, b), suggesting that growth rate decreases with increasing melt SiO_2 content.

Nucleation rates have also been estimated in basaltic (Burkhard 2005; Pupier et al. 2008), basaltic andesitic (Shea and Hammer 2013), and dacitic compositions (Hammer and Rutherford 2002; Brugger and Hammer 2010a, b). However, results vary substantially, ranging from 10^{-9} to 10^{5} cm^{-3} s^{-1}. These variations appear dependent not only on initial composition, but also on the characteristics of the starting material and the specific experimental procedure (e.g. synthetic vs. natural material, with/without superliquidus heating before cooling).

Furthermore, most experimental studies employed rapid cooling rates exceeding 10 °C/h (Nabelek et al. 1978; Conte et al. 2006; Iezzi et al. 2008; Vetere et al. 2015; Giuliani et al. 2020), which are probably adequate for the cooling of lava flows in contact with the atmosphere. Only a few studies have explored cooling rates slower than 7 °C/h (Pupier et al. 2008; Vetere et al. 2015; Giuliani et al. 2020), although magmas in deep, large reservoirs probably cool much slower than can be experimentally reproduced (Sunagawa 1977). For example, core samples from the Kilauea lava lake were interpreted to have cooled at rates of 0.002–0.011 °C/h (Honour et al. 2019).

Here, we experimentally determined plagioclase nucleation and growth rates in an anhydrous basaltic andesitic composition as a function of final (quench) temperature (T_f), nominal degree of undercooling ($-\Delta T_n$), and cooling time. Data from 20 new cooling experiments are presented. To best replicate natural conditions, a small density of pre-existing crystals was maintained in the starting material. We used a natural starting composition from Osorno volcano (Southern Volcanic Zone, Chile). To better approximate the gradual cooling of natural magma reservoirs (Mollo et al. 2012), we employed slow cooling rates of 1, 3, and 9 °C/h. As modeled by Mollo et al. (2012), this range allows for example to cover the progressive cooling of chilled magmatic intrusions (100–200 m thick) from the inner to outer part of the intrusion. We calculated nucleation and growth rates using different methods, then evaluated which method is the most appropriate for calculating storage timescales from textural analyses of volcanic samples.

Many experimental investigations have focused on constraining plagioclase crystallization parameters such as the rates of nucleation (J), growth (G; see Table 1 for variable definitions), and chemical equilibration (Gibb 1974; Nabelek et al. 1978; Toplis and Carroll 1995; Conte et al. 2006; Pupier et al. 2008; Brugger and Hammer 2010a, b; Vetere et al. 2015; Shea and Hammer 2013; Moschini et al. 2023). However, aside from the few direct observations of crystal growth rates using in situ X-ray tomography experiments in furnaces (e.g. Le Gall et al. 2021) or on heating stages (Schiavi et al. 2009), G and J are mostly estimated *post mortem* from polished sections using direct calculations or CSDs.

Methods

Starting material and experimental methodology

Our starting composition was a basaltic andesite (OS36 from Bechon et al. 2022) from Osorno volcano (Central Southern Volcanic Zone, Chile) (Table 2). OS36 is crystal-poor (containing only 9% crystals, and 2% plagioclase macrocrysts larger than 300 µm) and bubble-rich (19%) (Supplementary file 2). The sample was crushed with a hammer, then ground to a fine powder in an agate mortar with a Fritsch Pulverisette planetary mill.

To create the starting glasses, an aliquot of the starting powder was prepared as a pellet 1–3 mm in diameter and deposited on a 0.2-mm-diameter Pt wire loop. The Pt wire loops were previously equilibrated with material of the same composition as the experimental charge at the target temperature and oxygen fugacity ($Ni+1/2O_2=NiO$ equilibrium, NNO) for 24 h to minimize iron loss during the experiments (Grove 1981). The assemblage was then heated in a muffle furnace for 10–15 min to sinter the powder. All crystallization experiments were conducted at atmospheric pressure (1 atm) in a CARBOLITE GERO vertical furnace (ULiege) at NNO, close to the estimated oxygen fugacity

Table 1 Abbreviations used in this study

Abbreviations	
T_{liq}, T_{sat}	Phase-specific liquidus and saturation temperatures, respectively
T_i, T_f	Initial and final temperatures, respectively
$-\Delta T$, $-\Delta T_n$, $-\Delta T_{eff}$	True, nominal, and effective degrees of undercooling, respectively
l, w	2D major and minor axes of each plagioclase crystal, respectively
L, I, S	3D major, intermediate, and minor axes of each plagioclase crystal, respectively
Φ_V, Φ_{WDS}	Plagioclase proportions estimated from textural analyses and WDS measurments, respectively
S_N	Average plagioclase crystal size determined by the batch method
l_{mean}, w_{mean}	Average 2D size (major and minor axes, respectively) estimated over the section-wide segmented plagioclase population
$l_{max,avg}$, $w_{max,avg}$	Average 2D maximum sizes estimated from the 10 longest and largest crystals respectively
N_A, N_V	Areal and volumetric plagioclase crystal densities, respectively
n_0, l_c	2D initial density and characteristic size determined from the CSD, respectively
N_0, L_c	3D initial density and characteristic size determined from the CSD, respectively
J, G	Nucleation and growth rates, respectively
J_{batch}, $J_{CSD,2D}$, $J_{CSD,3D}$	Nucleation rates determined using batch and 2D and 2D CSD methods, respectively
J_{mean}	Average nucleation rate (mean of the results using the batch and 2D and 3D CSD methods)
G_{batch}	Growth rates determined by the batch method
$G_{mean,l}$, $G_{mean,w}$	Average growth rates determined from l_{mean} and w_{mean}, respectively
$G_{max,l}$, $G_{max,w}$	Maximum growth rates determined from $l_{max,avg}$ and $w_{max,avg}$, respectively
G_{rim}	Growth rate determined from crystal overgrowths
$G_{CSD,2D}$, $G_{CSD,3D}$	Growth rates determined using the 2D and 3D CSD methods, respectively
G_{mean}	Average growth rate
$t_{cooling/decompression}$	Cooling/decompression time after the initial step
CR, DP, ISO	Cooling rate, decompression rate, and isothermal experiments, respectively

(approximately QFM-QFM + 0.8/ + 1) for storage conditions under Osorno and other volcanoes of the area (Morgado et al. 2015; Vander Auwera et al. 2019; Bechon et al. 2022). Oxygen fugacity was controlled with CO-CO_2 gas. The temperature was measured using a S-type ($Pt_{90}Rh_{10}$-Pt) thermocouple with an accuracy of ± 3 °C at the hot spot of the furnace (± 4 cm).

Liquidus determination

Cooling experiments

Experiments were first heated to 1190 °C, i.e. 15 °C above the plagioclase saturation temperature (T_{sat} = 1175 °C), for 24 h. This step ensured that no new plagioclase grains formed during the initial heating stage, while retaining a small fraction of pre-existing crystals to initiate nucleation (Pichavant et al. 2007) (Fig. 2a; Supplementary file 2). Experiments were then cooled to various final temperatures (1175, 1165, 1140, 1120, or 1100 °C) at one of three cooling rates (1, 3, or 9 °C/h; Fig. 1) and quenched in water. The fastest cooling experiments were also extended to quenching temperatures of 1050 and 1000 °C (Fig. 1; Table 3). To test experimental reproducibility, experiments G 2–1 (3 °C/h, 1165 °C), and G 3–3 (9 °C/h, 1120 °C) were repeated twice.

Following Kirkpatrick (1981), Faure et al. (2003), and Faure and Tissandier (2014), we refer to the nominal degree of undercooling, $-\Delta T_n$, defined as the difference between the plagioclase saturation temperature in the starting composition (OS36) and the quench temperature ($-\Delta T_n = T_{sat} - T_f$). Accordingly, in our study, $-\Delta T_n$ ranged from 0 °C at the liquidus to 175 °C. However, Faure and Tissandier (2014) explained that this definition, particularly in the case of a slow cooling, corresponds to an oversimplification of the real undercooling ($-\Delta T$) which changes during cooling due to the progressive evolution of the melt composition.

Experimental runs were embedded in epoxy, polished, and examined with a scanning electron microscope (SEM) equipped with a field-emission gun source using backscattered electron imaging (BSE) at KU Leuven (TESCAN Mira4) and RWTH Aachen (FEI QEMSCAN 650F) (see Supplementary file 1 for operating conditions). Chemical analyses of the experiments were performed by energy dispersive X-ray analysis (EDS) and wavelength dispersive X-ray spectroscopy (WDS) following the protocol provided in Supplementary file 1.

Image processing

Data acquisition

BSE images of entire sections were used to determine the number of crystals in each section (between 100 and 3000 plagioclase crystals per section, ranging from > 2 to 333 µm, depending on crystallinity). For textural measurements, we outlined crystals in the BSE images. For better precision, especially for the smallest crystals (< 5 µm), the full images were subdivided into four to ten subsections (magnified by 160–750×) depending on the crystal density and sample

Table 2 Chemical compositions of the starting material (OS 36) and the residual liquid at each quench temperature (1190–1000 °C) during cooling at 1, 3 and 9 °C/h

	Bulk composition	ISO: 24 h		CR: 9 °C/h					
	OS36[a]	1190 °C[b]	1180 °C[b]	1165 °C[b]	1140 °C[b]	1120 °C[b]	1100 °C[b]	1050 °C[c]	1000 °C[c]
SiO_2	56.94	57.65 (1.07)	56.98 (0.20)	58.26 (0.50)	58.67 (0.56)	57.47 (0.79)	59.05 (0.70)	61.05 (1.25)	69.40 (1.34)
TiO_2	1.3	1.28 (0.04)	1.33 (0.09)	1.30 (0.07)	1.50 (0.11)	1.53 (0.07)	1.70 (0.07)	2.33 (0.32)	2.01 (0.42)
Al_2O_3	16.27	16.64 (0.16)	16.09 (0.17)	16.42 (0.18)	14.86 (0.64)	14.92 (0.35)	13.54 (0.26)	14.42 (0.83)	13.66 (1.00)
$FeO_{(t)}$	9.56	9.53 (0.90)	10.24 (0.47)	9.00 (0.31)	10.28 (0.87)	10.78 (0.63)	10.66 (0.80)	10.42 (1.01)	5.54 (0.77)
MnO	0.18	0.19 (0.03)	0.2 (0.03)	0.18 (0.03)	0.21 (0.05)	0.22 (0.03)	0.24 (0.04)	0.25 (0.04)	0.16 (0.03)
MgO	2.79	3.13 (0.15)	3.38 (0.04)	2.80 (0.12)	3.37 (0.25)	3.37 (0.65)	3.77 (0.13)	1.70 (0.14)	0.85 (0.21)
CaO	6.39	6.63 (0.37)	6.47 (0.22)	6.20 (0.20)	5.66 (0.19)	5.78 (0.24)	5.32 (0.21)	5.06 (0.39)	2.98 (0.51)
Na_2O	4.32	4.14 (0.08)	3.91 (0.09)	4.22 (0.10)	4.07 (0.16)	4.03 (0.14)	3.94 (0.18)	2.68 (0.10)	2.62 (0.42)
K_2O	0.91	0.89 (0.06)	0.93 (0.03)	0.97 (0.03)	1.05 (0.04)	1.02 (0.05)	1.11 (0.05)	1.56 (0.11)	2.16 (0.22)
P_2O_5	0.26	0.3 (0.03)	0.27 (0.03)	0.22 (0.05)	0.25 (0.06)	0.28 (0.05)	0.30 (0.08)	0.52 (0.09)	0.63 (0.07)
Total	98.92	100.38	99.79	99.58	99.93	99.56	99.62	99.99	100.01
Type		Andesitic	Andesitic	Andesitic	Andesitic	Andesitic	Andesitic	Andesitic	Dacitic
	CR: 1 °C/h					CR: 3 °C/h			
	1165[b] °C (Sample 1)	1165[b] °C (Sample 2)	1137[b] °C	1120[b] °C	1100[b] °C	1165[b] °C	1140[b] °C	1120[b] °C	1100[b] °C
SiO_2	57.03 (0.56)	57.99 (0.8)	59.61 (0.50)	58.36 (0.56)	59.08 (0.86)	57.77 (0.56)	57.83 (0.77)	58.42 (0.77)	57.67 (0.32)
TiO_2	1.36 (0.08)	1.31 (0.07)	1.44 (0.06)	1.52 (0.08)	1.68 (0.08)	1.28 (0.06)	1.51 (0.08)	1.57 (0.06)	1.60 (0.07)
Al_2O_3	15.92 (0.18)	16.08 (0.16)	15.13 (0.31)	13.81 (0.16)	13.57 (0.29)	16.39 (0.11)	15.05 (0.22)	14.43 (0.2)	13.14 (0.10)
$FeO_{(t)}$	9.69 (0.46)	9.03 (0.47)	8.87 (0.2)	9.59 (0.47)	10.19 (0.43)	8.83 (0.43)	10.35 (0.48)	10.35 (0.42)	11.09 (0.37)
MnO	0.2 (0.04)	0.19 (0.03)	0.18 (0.04)	0.23 (0.04)	0.22 (0.04)	0.18 (0.04)	0.22 (0.03)	0.21 (0.03)	0.26 (0.06)
MgO	3.17 (0.12)	2.89 (0.14)	3.02 (0.12)	3.77 (0.15)	3.6 (0.21)	2.95 (0.08)	3.39 (0.19)	3.49 (0.12)	4.10 (0.08)
CaO	6.22 (0.18)	5.9 (0.21)	5.17 (0.18)	5.47 (0.17)	5.02 (0.22)	6.13 (0.22)	6.02 (0.21)	5.43 (0.16)	5.53 (0.12)
Na_2O	4.08 (0.07)	4.06 (0.06)	4.38 (0.10)	4.16 (0.2)	4.13 (0.09)	4.18 (0.17)	4.00 (0.11)	3.86 (0.2)	3.82 (0.07)
K_2O	0.88 (0.03)	0.96 (0.05)	1.14 (0.03)	1.05 (0.05)	1.17 (0.05)	0.95 (0.04)	0.97 (0.05)	1.01 (0.04)	1.02 (0.03)
P_2O_5	0.2 (0.05)	0.25 (0.07)	0.21 (0.05)	0.21 (0.04)	0.27 (0.06)	0.24 (0.06)	0.27 (0.04)	0.28 (0.07)	0.30 (0.08)
Total	98.76	98.66	99.14	98.17	98.94	98.88	99.61	99.05	98.53
Type	Andesitic	Andesitic	Andesitic	Andesitic	Andesitic	Andesitic	Andesitic	Andesitic	Andesitic
Initial Conditions									
%wt H_2O	0								
P (bar)	1								
fO_2	NNO								

1σ errors are reported in parentheses

[a]XRF composition

[b]WDS measurements

[c]EDS measurements

heterogeneity of the sample. Because the BSE pixel size was about 0.5 µm on a side, we could only accurately measure crystals larger than 2 µm.

We first used the Weka Segmentation plugin of Fiji (ImageJ) to automate the outlining of the plagioclase crystals and their potential relic cores after adjusting the image contrast. Subsequently, the crystal outlines were verified, and each crystal was manually extracted from the images using GIMP software. The long (l) and short axes (w) of the outlined crystals were measured using the best-fit ellipse method in Fiji (see Supplementary file 4).

Textural parameters

We determined plagioclase proportions (φ_V), shape (see next subsection), sizes ($l_{max,avg}$ and $w_{max,avg}$ being the average dimensions respectively on the 10 longest and widest crystals; and l_{mean} and w_{mean} being the corresponding mean values of the entire crystal population in the section), and crystal number densities per unit area (N_A = number of crystals/surface area of the entire section) (Tables 1, 3). Using φ_V and N_A, we calculated the global mean crystal size (S_N) and volumetric crystal density (N_V) as (Hammer et al. 1999; Shea and Hammer 2013):

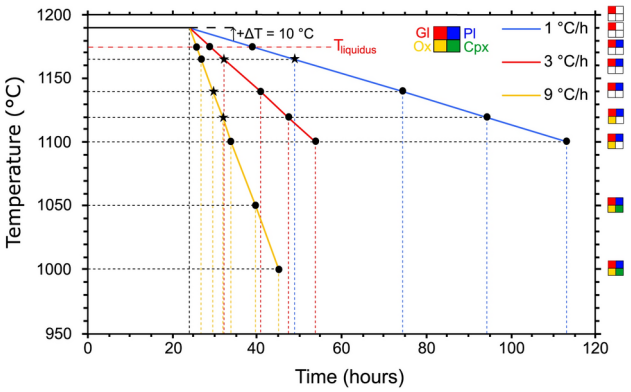

Fig. 1 The thermal paths of experiments in this study. The order in which phases appeared during cooling is indicated by the color code to the right of the diagram. Each experiment began with a 24-h isothermal heating step at 10 °C above the liquidus 24 h (run GERO 0) before cooling at 1, 3, or 9 °C/h and quenching at 1175 °C, 1165 °C, 1140 °C, 1120 °C, or 1100 °C; additional experiments cooled at 9 °C/h were also quenched at 1050 °C and 1000 °C. Stars indicate replicate experiments, either performed twice or with two samples during the same run

$$S_N = \sqrt{\frac{\varphi_V}{N_A}} \quad (1)$$

$$N_V = \frac{N_A}{S_N} \quad (2)$$

Plagioclase proportions and areal and volumetric number densities were measured from the global images of each section. Except for the experiments quenched at the beginning of crystallization at 1175 and 1165 °C, the crystal size parameters (l_{max}/w_{max}, $l_{max,avg}/w_{max,avg}$, and l_{mean}) were measured from the various subsectional images, and the results were then combined to derive the final data for the overall sample.

3D crystal shape

Crystal shapes imaged by SEM are 2D cross-sections of 3D objects, generally cut randomly. We used the algorithm ShapeCalc (Mangler et al. 2022) to estimate the 3D crystal shape (*S*:*I*:*L*; with *S*, *I*, and *L* being the 3D short, intermediate and long axes of elongation, respectively) based on the 2D width/length (*w*/*l*) distribution. Details on the algorithm are provided in Mangler et al. (2022).

Phase proportions

We used two methods to obtain phase proportions: 2D image processing (φ_V) reported in Table 3, and mass balance (φ_{WDS}) based on the WDS data (plagioclase and glass). The first method assumes that calculated phase proportions correspond to volume proportions (Delesse 1847; Brugger and Hammer 2010b). For the second method, we used densities as estimated by MELTS at the temperature of quenching (see Supplementary file 4). As highlighted by Vetere et al. (2024), the two methods gave similar results (absolute differences ranging between 1 and 4%, averaging around 1% and 2%). In the following, we use only the phase proportions obtained with 2D images processing (φ_V).

Crystal size distribution

Crystal Size Distribution (CSD) represents the total number of crystals $N(L)$ as a function of their size (L):

$$N(L) = \int_0^L n(L)d(L) \quad (3)$$

where *n(L)* corresponds to the number of crystals in each size range (L) per unit volume. In many magmatic systems, the plot of $N(L)$ vs. $\log(L)$ is a straight line with a negative slope (Cashman and Marsh 1988; Marsh 1988, 1998):

$$\ln(N(L)) = -L \times \frac{1}{G \times t} + \ln(N_0) \quad (4)$$

where N_0 is the number of crystal nuclei (crystals of zero length) and t is the duration below the saturation temperature of plagioclase (T_{sat} = 1175 °C). Assuming constant G (Armienti 2008; Marsh 1988, 1998), characteristic crystal size l_c, J, and G are determined as (with analogous equations for their 3D counterparts based on L_c):

$$l_c = G \times t \quad (5)$$

$$G_{CSD} = \frac{1}{\text{slope} \times t} \quad (6)$$

$$J_{CSD} = n_0 \times G_{CSD} \quad (7)$$

Additional details on the theory, methodology used and CSD data are provided in Supplementary files 1 and 4, respectively. The objective of this comparison was to observe the evolution of the CSD curves during progressive cooling, and also to extract the nucleation ($J_{CSD,2D}$ and $J_{CSD,3D}$) and growth ($G_{CSD,2D}$, $G_{CSD,3D}$) by linear regression.

Nucleation and growth rates

Nucleation and growth rates were calculated using different methods: the batch method (Brugger and Hammer 2010a, b), CSDs (2D and 3D; Burkhard 2002; Pupier et al. 2008), and the l_{mean} and l_{max} method (Shea and Hammer 2013). Rates derived from the log-linear segments of the CSDs are defined above (Eqs. 6 and 7). Maximum growth rates were

Table 3 Textural characteristics and image segmentation data

Name	Pre-treatment	Cooling rate (°C/h)	T_f (°C)	$-\Delta T_n$ (°C)[a]	$t_{final\ step}$ (h)	$t_{cooling}$ (h)	Phases	Global image				Segmentation			
								φ_v	N_A (μm^{-2})	S_N (μm)	N_V (μm^{-3})	$l_{max,avg}$[c] (μm)	$w_{max,avg}$[c] (μm)	l_{mean}[d] (μm)	w_{mean}[d] (μm)
Test 1	No	ISO	1175	0	24		Glass, Pl	–	–	–	–	–	–	–	–
Test 2	No	ISO	1180	− 5	24		Glass, P.c, Pl	–	–	–	–	–	–	–	–
Test 3	No	ISO	1185	− 10	24		Glass, P.c, Pl ?	–	–	–	–	–	–	–	–
G 0	No	ISO	1190	− 15	24		Glass, P.c[b]	<<0,01	2.23E-05	12	1.98E-06	36	22	16	11
Test 5	No	ISO	1200	− 25	24		Glass	–	–	–	–	–	–	–	–
Test 6	1450 °C for 2 h	ISO	1170	5	24		Glass, Pl	–	–	–	–	–	–	–	–
Test 7	1451 °C for 2 h	ISO	1180	− 5	24		Glass	–	–	–	–	–	–	–	–
Test 8	1452 °C for 2 h	ISO	1190	− 15	24		Glass	–	–	–	–	–	–	–	–
Test 9	1453 °C for 2 h	ISO	1200	− 25	24		Glass	–	–	–	–	–	–	–	–
G 1–0		1	1175	0	0	15.00	Glass. Pl	0.01	4.14E−05	16	2.59E−06	52	27	22	11
G 1-1a1		1	1165	10	0	25.00	Glass. Pl	0.06	2.55E−04	15	1.69E−05	87	41	21	10
No crystal corona		1	–	–	–	25.00	–	0.01	9.03E−05	11	8.58E−06	25	17	12	7
G 1-1a2		1	1165	10	0	25.00	Glass, Pl	0.03	1.62E−04	13	1.21E−05	68	34	21	10
G 1–2		1	1137	38	0	53.00	Glass, Pl	0.12	4.31E−04	17	2.54E−05	114	43	20	10
G 1–3		1	1120	55	0	70.00	Glass, Pl, Ox	0.21	4.99E−04	20	2.65E−05	130	42	23	9
No crystal corona		1	–	–	–	–	–	0.1	5.08E−04	14	3.62E−05	–	–	–	–
G 1–4		1	1100	75	0	90.00	Glass, Pl, Ox	0.21	5.63E−04	20	2.88E−05	183	56	26	11
G 2–0		3	1175	0	0	5.00	Glass, Pl	0.01	4.58E−05	13	3.61E−06	41	27	16	10
G 2-1a		3	1165	10	0	8.33	Glass, Pl	0.03	1.61E−04	14	1.16E−05	60	23	17	7
G 2-1b		3	1165	10	0	8.33	Glass, Pl	<<0,01	1.21E−05	15	7.95E−07	35	19	23	12
G 2–2		3	1140	35	0	16.67	Glass, Pl	0.11	3.73E−04	17	2.15E−05	135	40	24	9
G 2–3		3	1120	55	0	23.33	Glass, Pl	0.15	5.07E−04	17	2.97E−05	127	43	23	9
G 2–4		3	1100	75	0	30.00	Glass, Pl, Ox	0.2	5.30E−04	20	2.70E−05	156	45	27	10
G 3–0		9	1175	0	0	1.67	Glass, Pl	0.001	4.47E−06	16	2.87E−07	26	15	20	12
G 3–1		9	1165	10	0	2.78	Glass, Pl	0.01	1.63E−04	8	1.92E−05	31	20	10	5
G 3-2a1 (Seg1)		9	1140	35	0	5.56	Glass, Pl	0.14	7.05E−04	14	5.00E−05	123	35	18	7
G 3-2a1 (Seg2)		9	1140	35	0	5.56	Glass, Pl	0.14	7.05E−04	14	5.00E−05	103	33	18	7
G 3-2a2		9	1140	35	0	5.56	Glass, Pl	0.09	6.77E−04	12	5.75E−05	113	37	15	7
G 3-3a		9	1120	55	0	7.78	Glass, Pl	0.14	3.30E−04	21	1.58E−05	187	40	30	9
G 3-3b		9	1120	55	0	7.78	Glass, Pl	0.15	4.01E−04	19	2.11E−05	140	36	24	8
G 3–4		9	1100	75	0	10.00	Glass, Pl, Ox	0.24	8.81E−04	17	5.30E−05	126	42	21	8
G 3–5		9	1050	125	0	15.56	Glass, Pl, Ox, Cpx	0.39	5.69E−04	26	2.17E−05	133	46	35	13
G 3–6		9	1000	175	0	21.11	Glass, Pl, Ox, Cpx	0.48	–	–	–	103	39	35	14

[a]– ΔT_n = difference between the liquidus temperature and the final temperature

[b]P.c: Pre-existing crystals

[c]Average value on the 10 longest (l) and widest (w) crystals

[d]Average 2D long (l) and small (w) axis measured on the various zooms

derived from the average 2D length (l) and width (w) of the 10 longest crystals and 10 widest crystals ($G_{max,l}$, $G_{max,w}$) respectively:

$$G_{\max,l} = \frac{l_{\max,\ avg}}{2t}\ and\ G_{\max,w} = \frac{w_{\max,\ avg}}{2t} \quad (8)$$

Because many crystals displayed relic cores (Fig. 2b), we also calculated a growth rate based only on the overgrowth rim (G_{rim}; Shea and Hammer 2013) by subtracting the l and w axes of the ellipses fit to the relic cores from those of the total crystals. Seeds displaying resorbed textures, G_{rim} values refer only to the l axis.

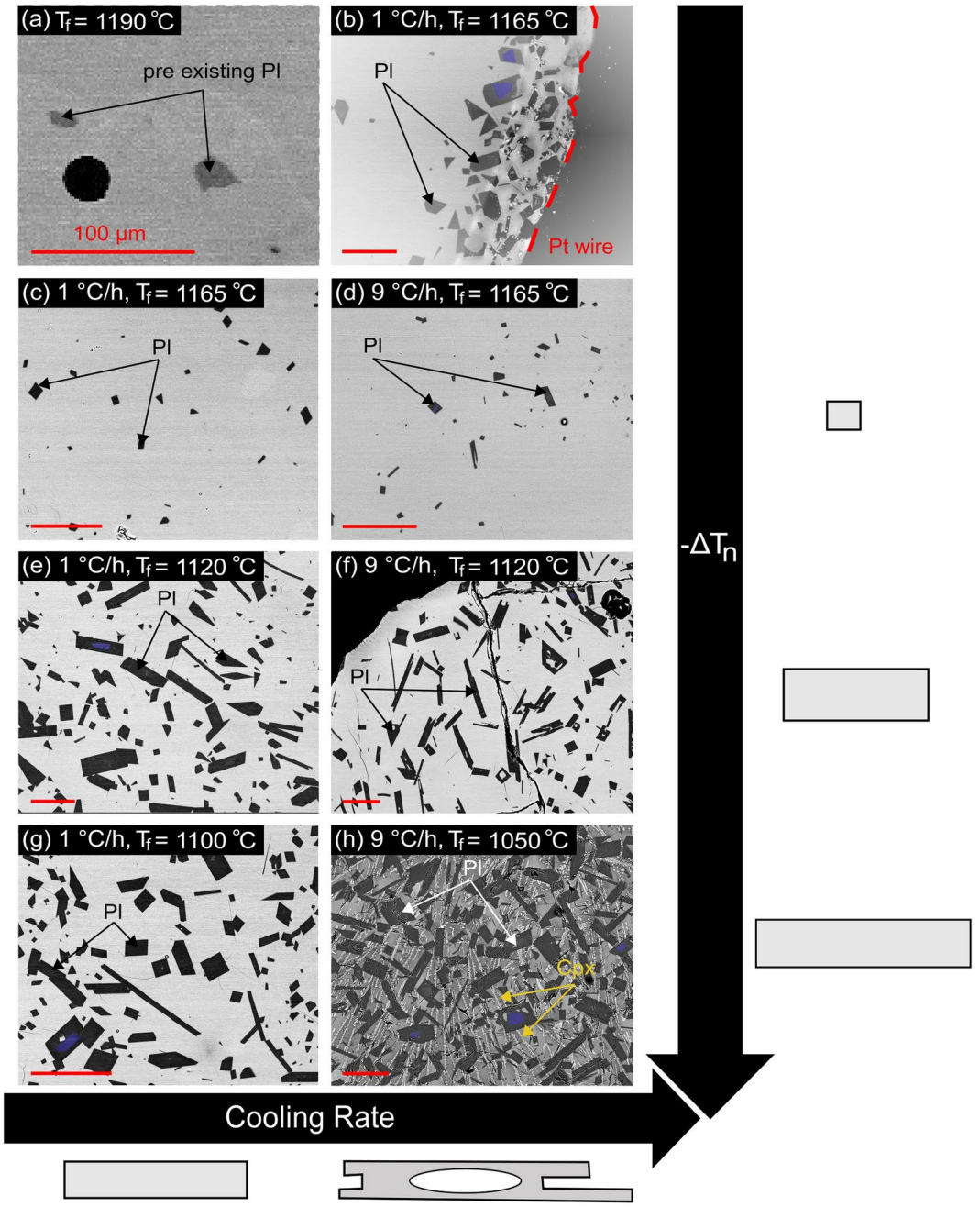

Fig. 2 Backscattered electron images documenting the textural evolution of plagioclase. **a** Primitive plagioclase relic cores observed at 1190 °C (ΔT = 10 °C), displaying a rounded texture indicative of resorption. **b**, **c**, **e**, **g** Textural evolution during cooling at 1 °C/h, showing a transition from small, equant crystals at 1165 °C (**c**) to larger, more tabular crystals at lower temperatures (**e** and **g**). **b** illustrates preferential nucleation, with larger plagioclase crystals forming near the Pt wire (marked by the red dashed line, later removed during polishing). **d**, **f**, **h** Textural evolution during cooling at 9 °C/h. Skeletal crystals appear at an intermediate stage (f: 1120 °C), coinciding with the increased cooling rate. At the most advanced stage of cooling (**h**), dendritic clinopyroxenes and oxides are observed. The blue shading in (**e**, **g**, and **h**) highlights the seed portions in some of the larger crystals

We obtained mean growth rates using the batch, l_{mean}, and CSD methods. $G_{\text{mean},w}$ and $G_{\text{mean},l}$ were calculated considering the average minor (w_{mean}) and major axis lengths (l_{mean}) lengths among the entire plagioclase population, respectively, as:

$$G_{\text{mean},l} = \frac{l_{\text{mean}}}{2t} \; and \; G_{\text{mean},w} = \frac{w_{\text{mean}}}{2t} \tag{9}$$

For comparison, G_{batch} was calculated using S_N and J_{batch} using N_V:

$$G_{\text{batch}} = \frac{S_N}{2t} \tag{10}$$

$$J_{\text{batch}} = \frac{N_V}{t} \tag{11}$$

For all methods, we assumed that crystallization occurred symmetrically on a given crystal face, and thus used the major and minor radii (respectively $\frac{l}{2}$ and $\frac{w}{2}$) of the best-fit ellipses.

Results

Phase assemblages and proportions

At 1190 °C (i.e. 15 °C above the liquidus), the experimental charges contained only resorbed anorthite-rich plagioclase grains, representing remnants of the initial starting powder (Fig. 2a). At lower temperatures, these remnant grains were observed to be enclosed within larger plagioclase crystals (Fig. 2b, e). Plagioclase was the only crystalline phase down to 60 °C below the liquidus, followed by Fe–Ti oxides (titanomagnetite) appearing between 1120 and 1100 °C, and clinopyroxene (Cpx) below 1050 °C (Fig. 2h). More broadly, below 1140 °C, sample textures are considered porphyritic (Fig. 2 e–h; Supplementary file 2). Pt wire (Fig. 2b) and gas bubbles, resulting from intergrain free volume that can trap CO–CO_2 gas, served as preferred nucleation sites for plagioclase crystals. Clustering increased with decreasing temperature (increasing $-\Delta T_n$), ranging from pairs of sintered crystals to well-developed plagioclase clusters containing many grains, suggesting agglomeration (Pupier et al. 2008). Although the distribution of plagioclase tends to gradually homogenize during cooling (with a more even distribution of individual crystals and clusters), it remains strongly heterogeneous above 1050 °C, with portions of the experiments dominated either by residual liquid or by crystals (individual crystals, clusters, or groups surrounding bubbles; e.g., at 1140 °C, Supplementary file 2). Finally, a "fully" homogeneous crystal distribution was only attained at advanced stages of crystallization at 1050 and 1000 °C.

The proportion of plagioclase increased with increasing $-\Delta T_n$, from 1 to 3% at T_f = 1165 °C ($-\Delta T_n$ = 10 °C) to 20–24% at 1100 °C ($-\Delta T_n$ = 75 °C) and 48% at 1000 °C ($-\Delta T_n$ = 175 °C; Table 3). Observed plagioclase proportions were within 1–4% of those predicted by Rhyolite-MELTS (Supplementary file 4). The proportion of plagioclase does not appear to have been influenced by cooling rate. Pyroxene proportions increased from 0% at T_f = 1100 °C to 15% and 31% at 1050 and 1000 °C, respectively, much higher than that predicted by Rhyolite-MELTS (8%). Fe–Ti oxides comprised a constant proportion of 1–2% from 1120 to 1000 °C.

Phase compositions

Mineral compositions

The composition of plagioclase as a function of temperature is presented in Fig. 3a. Resorbed plagioclase crystals were anorthite-rich, with compositions ranging from An_{70} to An_{89} (An = 100 × molar Ca/(Ca + Na)). We interpret these anorthite-rich cores as relics from the starting material because their compositions overlap those of resorbed crystals at 1190 °C and plagioclase cores ($An_{80–88}$) in the original sample OS36 (Bechon et al. 2022). During cooling, the anorthite contents of plagioclase overgrowths decreased from An_{62} at 1165 °C to An_{55} at 1100 °C (Fig. 3a). No significant compositional difference was observed between rims formed under different cooling rates, except at 1120 °C, where plagioclases crystallized at 9 °C/h had lower anorthite contents ($An_{55–57}$ vs. $An_{60–61}$ at 1 and 3 °C/h).

Oxide compositions were within the ranges 4–7 wt% TiO_2 and 71–75 wt% $FeO_{(t)}$. Some samples showed zoned distributions of Fe–Ti oxide compositions (e.g., sample G 1–3, 1 °C/h, 1120 °C; Supplementary file 2) suggesting a potential redox gradient within the charges (Fig. 3b). In sample G 1–4 (1 °C/h, 1100 °C), oxide compositions ranged from 7.13 ± 0.23 TiO_2 near the Pt wire, to 6.27 ± 0.04 in the inner part of the sample. However, these variations appear to depend on the sample. For instance, oxide compositions in sample G 1–3 ranged from 4.36 ± 0.16 wt% TiO_2 and 74.40 ± 0.43 wt% $FeO_{(t)}$ at the edge, to 4.70 ± 0.13 wt% TiO_2 and 75.32 ± 0.41 wt% $FeO_{(t)}$ at the core.

Melt composition

The melt composition ranged from andesitic (57–59 wt% SiO_2, ~5 wt% $Na_2O + K_2O$) at the liquidus to dacitic (67–71 wt% SiO_2, ~4.5–5 wt% $Na_2O + K_2O$) at 1000 °C (Table 2). Cooling led to a slight decrease in CaO and Al_2O_3 contents

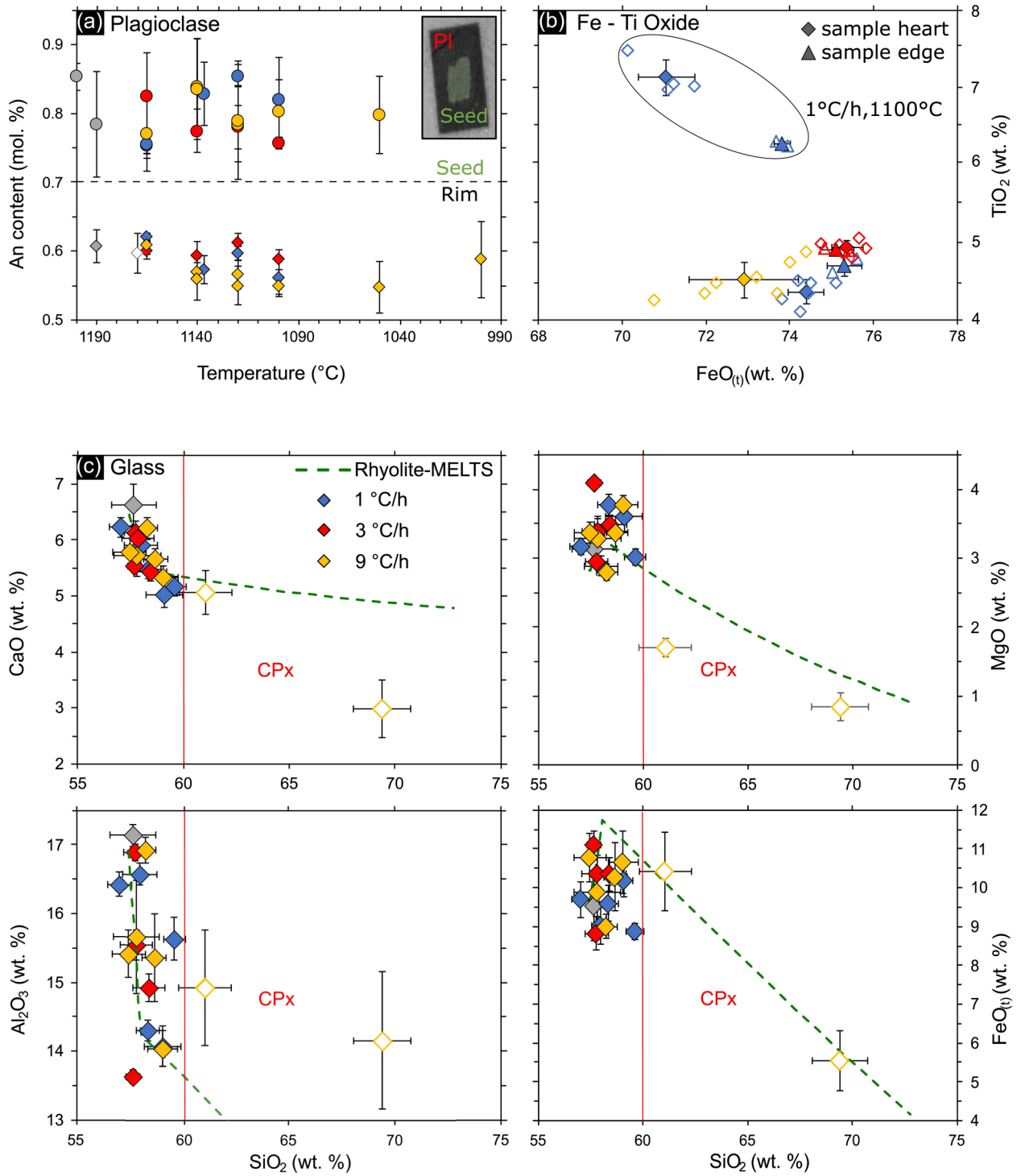

Fig. 3 The evolving chemical compositions of **a** plagioclase, **b** Fe–Ti oxides, and **c** the residual melt. **a** An content in plagioclase rims and cores vs. temperature (open symbols, WDS data; filled symbols, EDS data). Error bars correspond to the minimum and maximum values obtained for each sample. Rim An contents slightly decreased with decreasing temperature. **b** $FeO_{(t)}$ vs. TiO_2 in Fe–Ti oxides. Results are shown for crystals in the sample center and for those near the sample edge. Filled symbols indicate average values calculated from the individual point measurements (unfilled symbols). Error bars are 1σ errors. **c** CaO, Al_2O_3, MgO, and FeO contents vs. SiO_2 content in the experimental melts. The red vertical line indicates the appearance of Cpx in the experiments

due to plagioclase crystallization (Fig. 3c). Aside from slightly lower Al_2O_3 and CaO contents near the sample edge and the Pt-wire (where plagioclase crystals were most abundant), the melt composition was homogeneous (Supplementary file 3). The concentration of other elements remained generally constant during crystallization. At 1050 and 1000 °C, pyroxene crystallization induced a slight decrease of FeO and MgO contents in the melt. We did not observe clear trends in liquid composition as a function of cooling rate (Fig. 3c).

Microstructural variations

Plagioclase grain shapes ranged from anhedral and resorbed relic crystals near the liquidus to euhedral during cooling (Fig. 2). Most experiments displayed well-faceted crystals with well-defined prismatic/tabular shapes, corresponding to interface-controlled growth at low degrees of undercooling (Fig. 2c, e, g). However, experiments cooled at 9 °C/h, especially those quenched at 1120 °C, contained hollow/skeletal plagioclase crystals (Fig. 2d, f; Supplementary file 2). Fe–Ti oxides and clinopyroxenes in those experiments also exhibited skeletal/dendritic textures, indicating diffusion-limited growth consistent with rapid growth at high degrees of undercooling (Fig. 2h, Supplementary file 2).

Crystal density and size parameters

The liquidus temperature of OS36 was calculated using Rhyolite-MELTS v. 1.2.0 (Gualda et al. 2012) to be 1170 °C (1 atm, anhydrous, NNO). We tested this liquidus estimate using two series of experiments (Table 3): (1) a series of five isothermal experiments run between 1175 and 1200 °C for 24 h, and (2) a similar series using a powder previously preheated to 1450 °C for 2 h to ensure the complete absence of crystal seeds in the starting material. The first set of experiments showed plagioclase saturation at 1185 ± 5 °C and the complete dissolution of all pre-existing crystals at 1200 °C. In the second set of experiments, we estimated the saturation temperature of plagioclase to be around 1170–1175 °C, indicating that the presence of crystal seeds may lead to plagioclase saturation at a slightly higher temperature.

The volumetric proportion (φ_V) and sizes of crystals (l_{max}), as well as their number densities (N_A), increased with increasing $-\Delta T_n$ (Fig. 4a–d) down to 1050 °C. The apparent decrease in crystal size (Fig. 4d) between 1050 and 1000 °C can be explained by (i) a higher crystal content, leading to the formation of more equant crystals, or (ii) excessively high crystallinity, making segmentation more difficult and uncertain. The relatively high values of S_N and l_{max} at 1175 °C (G 1–0, G 2–0, G 3–0) are explained by an initial stage involving growth on pre-existing crystal seeds,

Fig. 4 Textural data from the cooling experiments. **a**, **b** Volumetric proportion of plagioclase (ϕ_V) as functions of the **a** temperature and **b** cooling time ($t_{cooling}$). **c**, **d** Crystal number density per unit area (N_A) and the average maximum crystal sizes ($l_{max,avg}$, averaged from the 10 largest crystals), respectively, as functions of the plagioclase proportion (as a measure of crystallization progress). **e** 2D aspect ratio (w/l) vs. maximum (longest) crystal size (l_{max}). **f**, **g** Proportions of plagioclase crystals binned as a function of w/l for different **f** quench temperatures and **g** cooling rates. In **e**–**g**, 2D crystal sketches illustrate w/l. Because the temperature and plagioclase proportion are directly linked, the x-axis in **c** and **d** is the plagioclase proportion, highlighting the linear relationship observed at 1 and 3 °C/h. Multiple symbols for the same run conditions (e.g. cooled at 9 °C/h and quenched at 1140 °C) correspond to replicate experiments. Symbol colors indicate cooling rate except in (**e**), where cooling rates are not indicated, and (**f**), where colors indicate quench temperature

forming larger crystals than those that newly nucleated (Table 3). Experiments cooled at 1 °C/h and 3 °C/h showed a more rapid and linear increase in size and number density at low to moderate $-\Delta T_n$ (10–35 °C), with a break in slope below 1140–1120 °C ($\varphi_V = 0.11$–0.15). Despite a more scattered evolution of the number density at 9 °C/h, a similar trend was observed, with the highest N_A values exceeding 4×10^{-4} μm^{-2} at 1140 °C (Fig. 4c). The anomalously low N_A values (3–4×10^{-4} μm^{-2}) in the experiments quenched at 1120 °C were related to the presence of skeletal crystals. Contrary to the observations of Conte et al. (2006), we found no clear relationship between crystal size and cooling rate, except in experiments quenched at 1100 °C, in which l_{max} decreased with increasing cooling rate (Table 3).

2D morphology

Crystal sizes and shapes (quantified as the aspect ratio w/l) varied significantly within each experimental charge. Although we observed no distinct mode of 2D aspect ratio (w/l) between 1140 and 1100 °C, the ratio generally decreased with increasing $-\Delta T_n$, as illustrated by an increasing proportion of crystals with $w/l < 0.3$–0.4 at lower quenching temperatures (Fig. 4f). This global evolution from equant to tabular shapes was associated with increased crystal size (Fig. 4e; Supplementary file 4). Crystals larger than 100 μm were characterized by $w/l < 0.25$. Despite some variations, at a given temperature the 2D aspect ratio tended to decrease with increasing cooling rate (Fig. 4g); for example, at 1100 °C the proportion of crystals with $w/l = 0.6$–1.0 was lower in experiments cooled at 3 °C/h and 9 °C/h than in those cooled at 1 °C/h, whereas the proportion of crystals with $w/l = 0.1$–0.4 was higher.

3D shape

3D crystal shapes are classified as equant ($S=I=L$), elongated/oblong ($S=I<L$), prismatic/bladed ($S<I<L$), or

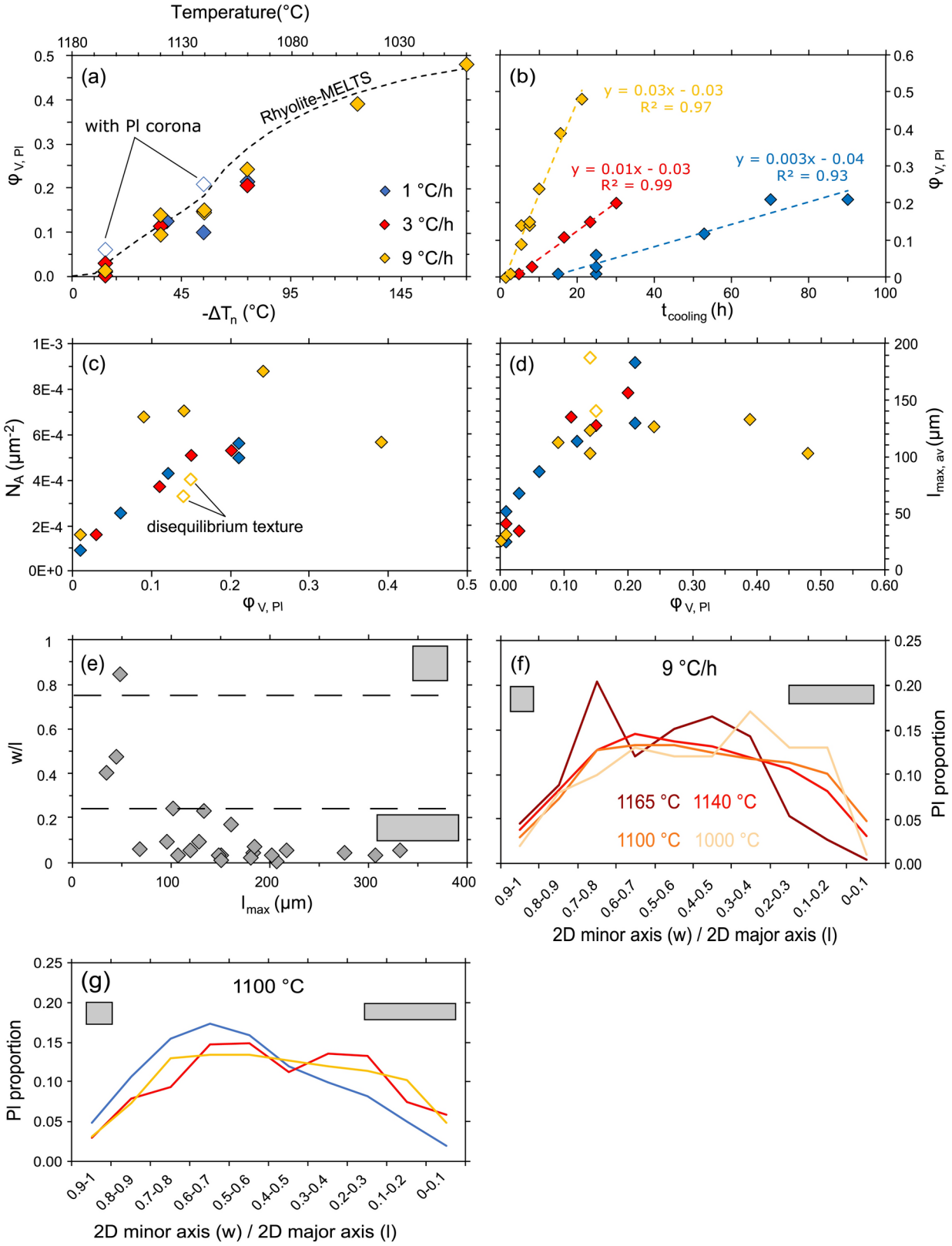
Temperature(°C)
1180
1130
1080
1030
(a)
with Pl corona
Rhyolite-MELTS
1 °C/h
3 °C/h
9 °C/h
φ V, Pl
-ΔT n (°C)
(b)
y = 0.03x - 0.03
R² = 0.97
y = 0.01x - 0.03
R² = 0.99
y = 0.003x - 0.04
R² = 0.93
t cooling (h)
(c)
disequilibrium texture
N A (µm-2)
(d)
l max, av (µm)
(e)
w/l
l max (µm)
(f)
9 °C/h
1165 °C 1140 °C
1100 °C 1000 °C
Pl proportion
2D minor axis (w) / 2D major axis (l)
(g)
1100 °C

tabular ($S<I=L$), and are presented in Zingg diagrams (I/L vs. S/I; Zingg 1935) (Fig. 5; Supplementary file 4). Except for experimental charges cooled at 9 °C/h, characterized by elongated skeletal crystals at 1120 °C, there is no clear variation in 3D shape with increasing $-\Delta T_n$ from 40 to 80 °C. Only a small decrease in S/I and increase in I/L was observed when considering the entire crystal population of each experiment (Fig. 5a). The 3D shape (S/I) decreased from 0.8 to 0.65 at 1 °C/h, and from 0.65 to 0.55 at 3 °C/h. The only exception to this trend is for experiments at 1190 °C, 1175 °C and 1165 °C, which were above or very near the liquidus, and at 1050 °C, corresponding to an advanced step of crystallization ($S/I=0.37$, $I/L=0.48$).

Considering distinct ranges of crystal sizes, crystal shapes were generally correlated with increasing crystal size (Fig. 5b): the smallest crystals were equant to elongated (i.e. $w/l=0.7$–0.8 at 1165 °C). This evolution from equant to elongated shapes mainly occurred along the long axis, decreasing I/L. The main growth stage to larger tabular/bladed crystals ($w/l=0.4$–0.5 at 1120 and 1100 °C) occurred along the intermediate axis (decreasing S/I). Finally, the largest crystals (>100 µm) had prismatic/tabular shapes ($w/l=0.3$–0.1) and, at high $-\Delta T_n$ (1100 °C), were nearly equant to tabular, with $I=L$.

Crystal size distributions

CSDs plotted with and without 3D correction were quite similar; accordingly, we focus on CSDs without 3D correction (see ***Supplementary file 4*** for the various CSD parameters). Although the nucleation number densities of the smallest crystals and the y-axis intercept changed by 10–25% when using CSDCorrections, all curves displayed the same overall shape commonly observed in most experimental (Pupier et al. 2008; Brugger and Hammer 2010b) and natural studies (Cashman and Marsh 1988; Marsh 1998): CSDs comprised a prominent log-linear, negatively sloped segment extending from 10–15 to 95 µm at 1165 °C and to 145 µm at 1100 °C, followed by a shallowly sloped segment corresponding to the largest crystals (Supplementary file 4) that can be attributed to fewer measured crystals or variable growth rates. A strong upward (convex) curvature, i.e. a positive slope at the smallest crystal sizes (≤5–10 µm), was observed in several runs.

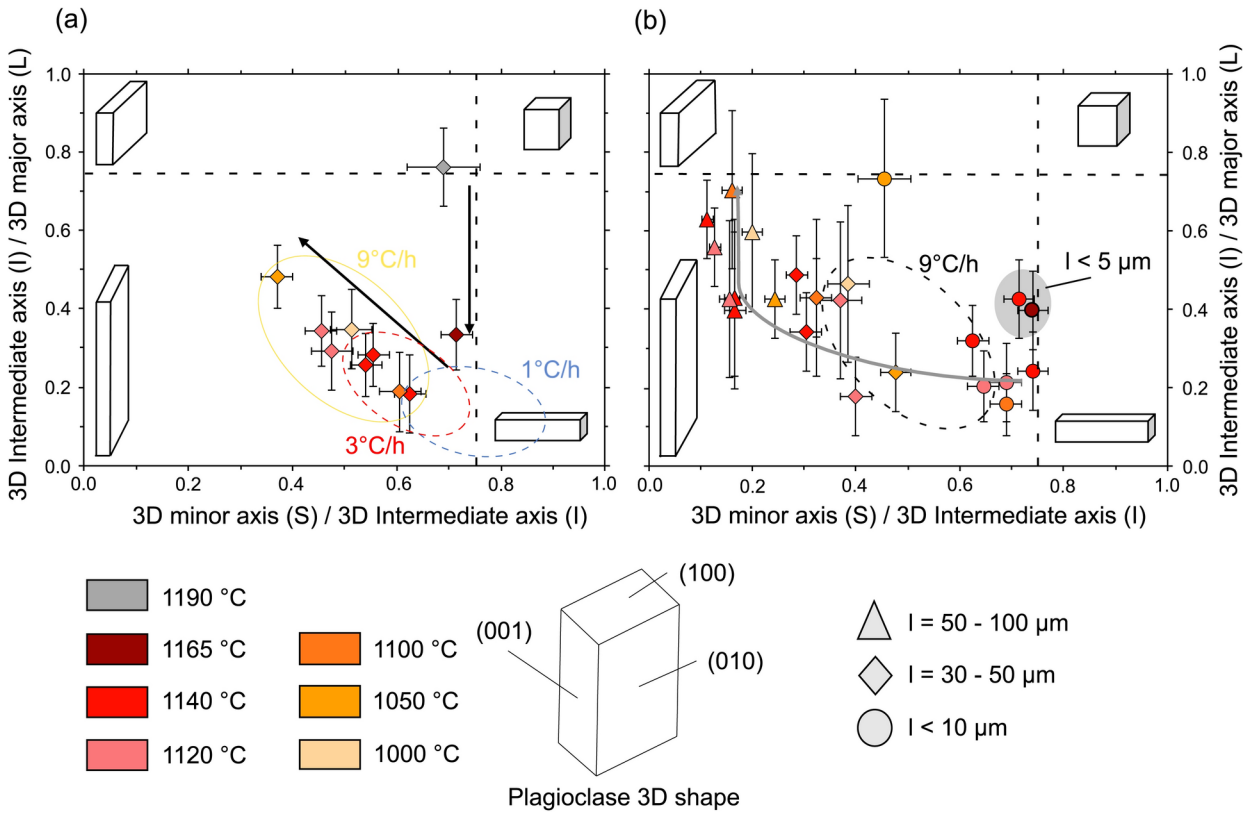

Fig. 5 Zingg diagrams of G-3 runs (cooling rate=9 °C/h) using the 3D shapes ($S:I:L$) calculated with Shapecalc (Mangler et al. 2022). **a** 3D shape evolution considering all G-3 samples. Bue and red dashed ellipses indicate the ranges of values for runs cooled at 1 and 3 °C/h, respectively, but individual data points are not shown here. **b** 3D shapes of distinct crystal size populations. Similar results are shown for the other series of experiments in Supplementary Material 3

The evolutions of the characteristic size (l_c) and intercept (ln (n_0) for $l=0$) were globally consistent with microstructural evolutions (see section above). For the same cooling rate, the slope of the log-linear part of the CSDs flattened as T_f decreased, marking an increase of l_c (Supplementary file 4). This increase in crystal size seems to be linked to the increased cooling time. Despite very small increases of the intercepts at cooling rates of 1 and 3 °C/h (by 8 and 3% respectively), the maximum crystal density was reached at 1140 °C (cooling at 9 °C/h) or 1120 °C (cooling at 1 and 3 °C/h), followed by a decrease with increasing cooling time (Supplementary file 4). A stagnation of the initial crystal density with a relative difference of the intercept value ranging from 1 and 3% is noted between 1140 and 1100 °C. As mentioned above, the decreased intercept at 1050 and 1000 °C (i.e. at advanced stages of crystallization) correlated with a sharp decrease in the proportion of crystals smaller than 10 µm.

Considering l_{max} and N_A, fluctuations of the CSD intercept value, especially at 9 °C/h and 1120 °C, reflect a change from tabular/prismatic to skeletal crystal shapes. More generally, runs cooled at 9 °C/h displayed lower l_c values and higher intercept values (Supplementary file 4). This observation is linked to the instantaneous degree of undercooling, which increases with increasing cooling rate. The CSD parameters (l_c, ln(n_0)) obtained at 1 and 3 °C/h were similar, particularly the intercept values.

Nucleation and growth rates

Nucleation and growth rates ranged from 1.66×10^{1} to 6.33×10^{3} cm^{-3} s^{-1} and from 2.04×10^{-9} to 4.39×10^{-7} cm/s, respectively (Table 4), similar to the rates obtained by Pupier et al. (2008) at comparable cooling rates. Both J and G followed similar trends (Fig. 6a), with an initial increase just below the liquidus to a maximum at 1165 °C (runs cooled at 1 or 3 °C/h) or 1140–1120 °C (9 °C/h), before gradually decreasing by nearly half an order of magnitude.

Between the series cooled at 1 and 9 °C/h, nucleation rates increased by more than 1 order of magnitude, and growth rates by a factor of 8 (Supplementary file 5). However, the rates measured depend on the method used (Table 4; Fig. 6b). Average growth rates ranged from 1.00×10^{-7} to 3.70×10^{-9} cm/s using the batch method, from 1.25×10^{-7} to 4.81×10^{-9} cm/s considering the entire, segmented population (l_{mean}), and from 4.39×10^{-7} to 3.28×10^{-8} cm/s based on l_{max}, the latter being 1 order of magnitude higher than the rates calculated using the batch and l_{mean} methods. Similarly, nucleation rates ranged from 4.80×10^{3} to 6.63×10^{1} cm^{-3} s^{-1} with the batch method and from 1.33×10^{3} to 1.66×10^{1} cm^{-3} s^{-1} with the 3D CSD method. All rates are reported in Table 4. The growth rates obtained from G_{mean} and G_{max} along the 2D major axis (l) were respectively 2.22 ($R^2=0.97$) and 2.52 ($R^2=0.87$) times higher than those obtained from the 2D minor axis (w), suggesting axis-dependent growth (Pupier et al. 2008; Mangler et al. 2022).

Experimental reproducibility

To confirm the reproducibility of our results, several experiments were replicated in separate runs (3 °C/h and 1165 °C, runs G 2-1a and b; 9 °C/h and 1120 °C, runs G 3-3a and b). In addition, in some cases, we included two separate samples in the same runs (1 °C/h and 1165 °C, runs G 1-1a1 and a2; 9 °C/h and 1140 °C, runs G 3-2a1 and a2). Except for experiments G 2-1a and b (1165 °C, 3 °C/h), the textural parameters (texture data, 2D aspect ratio, CSD parameters, and nucleation and growth rates) in replicated experiments were very similar (Supplementary file 4), demonstrating good reproducibility.

The overall crystal distributions, as well as the distributions of the 2D aspect ratio w/l were very similar, with relative differences of 1–36%. Similar reproducibility values were obtained for the textural data and CSD parameters. In contrast, G 2–1 replicates at 1165 °C showed relative differences of 92–93% for N_A/N_V and J_{batch}; this gap is attributed to semi-random nucleation near the liquidus, partly due to the random density and distribution of pre-existing crystal seeds. To assess uncertainties related to image segmentation, experiment G 3-2a1 (9 °C/h, 1140 °C) was segmented twice. The differences observed in this comparison were generally 2% for textural and CSD data and 14% for nucleation and growth rates. The largest deviations (28%) are attributed to segmentation of the smallest crystals and the associated determination of their aspect ratios.

Discussion

Crystallization kinetics

The small number of surviving seeds after 24 h at 1190 °C, and their resorbed textures, indicate that the crystal seeds were not in chemical equilibrium with the melt. The appearance of less calcic overgrowths on seeds suggests a rapid stabilization of plagioclase during the first 2 h of cooling (at 9 °C/h, $T_f=1175$ °C).

Nucleation mechanisms

The higher proportion of plagioclase grains with cores corresponding to seeds from the initial crystal population compared to completely newly formed crystals at 1175 °C

Table 4 Nucleation (cm^{-3} s^{-1}) and growth (cm s^{-1}) rates calculated by various methods

			Growth rate (cm s^{-1})								Nucleation rate (cm^{-3} s^{-1})			
Sample	Cooling rate (°C/h)	T_f (°C)	G_{Batch}	$G_{mean, w}$	$G_{mean, l}$	$G_{CSD, 2D}$	$G_{CSD, 3D}$	$G_{max, l}$	$G_{max, w}$	G_{rim}	J_{Batch}	$J_{CSD, 2D}$	$J_{CSD, 3D}$	J_{mean}
G 1–1 (sample 1)	1	1165	2.08E−08	1.39E−08	2.92E−08	1.40E−08	4.57E−08	1.21E−07	5.69E−08	2.56E−08	4.69E+02	4.65E+02	9.57E+01	2.59E+02
No crystal corona	1	1165	1.53E−08	9.72E−09	1.67E−08	6.94E−09	3.13E−08	3.47E−08	2.36E−08	–	2.38E+02	1.43E+03	1.90E+02	4.66E+02
G 1–1 (sample 2)	1	1165	1.81E−08	1.39E−08	2.92E−08	1.53E−08	5.79E−08	9.44E−08	4.72E−08	–	3.36E+02	2.64E+02	4.84E+01	1.63E+02
G 1–2	1	1137	6.21E−09	3.65E−09	7.31E−09	3.85E−09	1.54E−08	4.17E−08	1.57E−08	8.61E−09	1.86E+02	1.87E+02	3.88E+01	1.04E+02
G 1–3	1	1120	5.05E−09	2.53E−09	5.81E−09	2.27E−09	1.25E−08	3.28E−08	1.06E−08	9.72E−09	1.34E+02	1.19E+02	2.49E+01	7.07E+01
G 1–4	1	1100	3.70E−09	2.04E−09	4.81E−09	2.59E−09	9.74E−09	3.39E−08	1.04E−08	6.67E−09	1.07E+02	8.40E+01	1.66E+01	5.30E+01
G 2–1 (sample 1)	3	1165	5.83E−08	2.92E−08	7.08E−08	3.61E−08	1.20E−07	2.50E−07	9.58E−08	8.42E−08	9.67E+02	1.17E+03	2.87E+02	6.09E+02
G 2–1 (sample bis)	3	1165	6.25E−08	5.00E−08	9.58E−08	–	–	1.46E−07	7.92E−08	–	6.63E+01			3.52E+01
G 2–2	3	1140	2.02E−08	1.07E−08	2.86E−08	1.43E−08	4.43E−08	1.61E−07	4.76E−08	3.33E−08	5.12E+02	4.77E+02	1.17E+02	2.78E+02
G 2–3	3	1120	1.29E−08	6.82E−09	1.74E−08	8.33E−09	2.12E−08	9.62E−08	3.26E−08	2.69E−08	4.50E+02	4.30E+02	1.34E+02	2.55E+02
G 2–4	3	1100	1.11E−08	5.56E−09	1.50E−08	6.39E−09	1.53E−08	8.67E−08	2.50E−08	2.31E−08	3.00E+02	2.81E+02	8.70E+01	1.68E+02
G 3–1	9	1165	1.00E−07	6.25E−08	1.25E−07	7.50E−08	1.73E−07	3.88E−07	2.50E−07	1.13E−07	4.80E+03	2.77E+03	9.83E+02	2.14E+03
G 3–2 (sample 1) Seg 1	9	1140	5.00E−08	2.50E−08	6.43E−08	3.04E−08	8.10E−08	4.39E−07	1.25E−07	–	3.57E+03	5.55E+03	1.25E+03	2.59E+03
G 3–2 (sample 2)	9	1140	4.29E−08	2.14E−08	5.36E−08	2.99E−08	9.49E−08	4.04E−07	1.32E−07	7.75E−08	4.11E+03	6.33E+03	1.19E+03	2.91E+03
G 3–2 (sample 1) Seg 2	9	1140	5.00E−08	2.50E−08	6.43E−08	3.21E−08	8.26E−08	3.68E−07	1.18E−07	–	3.57E+03	4.60E+03	1.33E+03	2.38E+03
G 3–3 (sample 1)	9	1120	4.77E−08	2.05E−08	6.82E−08	2.05E−08	7.04E−08	4.25E−07	9.09E−08	9.08E−08	7.18E+02	1.27E+03	2.38E+02	5.58E+02
G 3–3 (sample bis)	9	1120	4.32E−08	1.82E−08	5.45E−08	1.36E−08	7.44E−08	3.18E−07	8.18E−08	–	9.59E+02	2.27E+03	3.00E+02	8.83E+02
G 3–4	9	1100	2.83E−08	1.33E−08	3.50E−08	1.67E−08	5.76E−08	2.10E−07	7.00E−08	4.22E−08	1.77E+03	2.22E+03	4.84E+02	1.12E+03
G 3–5	9	1050	2.60E−08	1.30E−08	3.50E−08	2.00E−08	3.29E−08	1.33E−07	4.60E−08	–	4.34E+02	4.82E+02	2.14E+02	2.84E+02
G 3–6	9	1000		1.00E−08	2.50E−08	1.25E−08	3.09E−08	7.36E−08	2.79E−08	–		3.17E+02	1.18E+02	2.17E+02

suggests that growth primarily occurs on pre-existing crystals rather than on newly formed nuclei at the lowest degrees of nominal undercooling ($-\Delta T_n$). This is consistent with the large activation energy required for plagioclase nucleation, as well as the decreasing critical size of the atom clusters needed to form stable nuclei with increasing degrees of undercooling (Berkebile and Dowty 1982; Hammer 2008; Shea and Hammer 2013). The slightly variable crystal densities observed in experiments quenched at low degrees of effective undercooling (e.g. samples cooled at 3 °C/h and quenched at 1165 °C) suggest erratic nucleation at the beginning of crystallization, potentially due to an inhomogeneous distribution of seeds in the starting material. Previous studies (Gibb 1974; Sato 1995; Fokin et al. 2006; Hammer 2008) argued that sufficiently fast cooling rates can cool the melt faster than the time necessary for the unrelaxed structure of the melt to 'rebalance' and enable nucleation. The resultant incubation period could explain the sharp decrease in newly formed crystals with increased cooling rate at 1175 °C.

The abundance of large crystals both around the platinum wire and at the surface of gas bubbles indicates that heterogeneous nucleation occurred (e.g. Lofgren 1983; Nabelek et al. 1978; Pupier et al. 2008; Shea and Hammer 2013). As noted by Corrigan (1982a, b), the random configuration of the Pt wire within each sample can generate spatially variable heterogeneous nucleation, contributing to the inhomogeneous distribution of crystals often observed in our experiments. Such heterogeneous nucleation, which is particularly evident at low degrees of undercooling ($-\Delta T_n$ = 0–10 °C), was also present during crystallization at lower temperatures ($-\Delta T_n$ = 35–75 °C), with Fe–Ti oxide grains nucleating at the contact with Pt wire. However, the difficulty in obtaining material from the experimental charge in direct contact with the Pt wire prevents us from determining whether this trend continues through the most advanced stages of crystallization at 1050 and 1000 °C ($-\Delta T_n$ = 125–175 °C).

The absence of both crystal clusters and a preferential crystal spatial distribution in the sample center at 1165 °C ($-\Delta T_n$ = 15 °C) suggests that homogeneous nucleation also occurred, although this is difficult to verify because heterogeneous nucleation can occur even on sub-microscopic particles. The absence of an initial strong superheating step ($+\Delta T$ = 15 °C) in our experiments likely preserved nanometric plagioclase nuclei (as observed by Burkhard (2005), which can act as substrates for nucleation. Accordingly, the pronounced curvature in our CSDs between 1140 and 1100 °C (Supplementary file 4) suggests that 70–98% of crystals nucleated via heterogeneous nucleation (Špillar and Dolejš 2015).

With decreasing temperature from 1140 to 1100 °C, the number of plagioclase clusters increased in our experiments. These were formed either by the relative movement of nearby but previously isolated crystals, or through secondary nucleation upon the breakage of pre-existing crystals when impinged by neighboring crystals as crystal density increased. The dendritic pyroxene crystals radiating from plagioclase grains ($-\Delta T_n$ = 125 and 175 °C) were most likely due to the heterogeneous nucleation of pyroxene on plagioclase (Rusiecka et al. 2020; Walker et al. 1978; Shea and Hammer 2013). Similarly, clinopyroxene acts as a nucleation substrate for Fe–Ti oxides, with many oxides crystallizing on clinopyroxene edges (Griffiths et al. 2023). Heterogeneous nucleation was thus a dominant process in our experiments, which therefore compare rather well to magma reservoirs (Cashman and Marsh 1988), in which xenocrysts and antecrysts are common (e.g. Sunagawa 1981; Berkebile and Dowty 1982; Lofgren 1983).

Plagioclase growth mechanisms

Interface-controlled growth (limited by reactions at the crystal-melt interface) typically produces euhedral crystals (Watson and Liang 1995), whereas diffusion-controlled growth (limited by the diffusion of components from the melt to the interface) results in skeletal to dendritic shapes (Kirkpatrick 1975, 1981; Sunagawa 1981; Watson 1996). Recently, Mangler et al. (2023) proposed an additional intermediate growth regime for euhedral crystals, in which melt-interface reactions and melt diffusivities compete. Here, the growth of the longest 2D dimension (with the faster interfacial reaction rate) is limited by the melt diffusion rate, resulting in reduced growth along the 2D major axis (l) compared to the 2D minor axis (w). Crystals growing in this regime become more compact (increasing w/l) and can develop hopper or swallowtail textures as diffusion becomes the limiting factor. As explained above, at low nominal undercooling ($-\Delta T_n$ = 0–10 °C), slow nucleation favors overgrowth on pre-existing crystals. Indeed, at slow cooling rates of 1–3 °C/h, corresponding to low degrees of undercooling between 15 and 80 °C, euhedral/equant to prismatic or tabular plagioclases and Fe–Ti oxides were observed, suggesting interface-controlled growth.

At a faster cooling rate of 9 °C/h, corresponding to an increased degree of undercooling, the transition from euhedral crystals to hopper (1165 and 1140 °C) and swallowtail habits (particularly visible at 1120 °C) suggests predominantly diffusion-controlled growth (e.g. Lofgren 1974; Kirkpatrick 1975; Hammer and Rutherford 2002; Couch et al. 2003a; Shea and Hammer 2013). The intermediate growth regime of Mangler et al. (2023) can explain the evolution from tabular to compact and, eventually, swallowtail habits when diffusion becomes the rate-limiting mechanism of growth along 2D longest axis. However, the significant

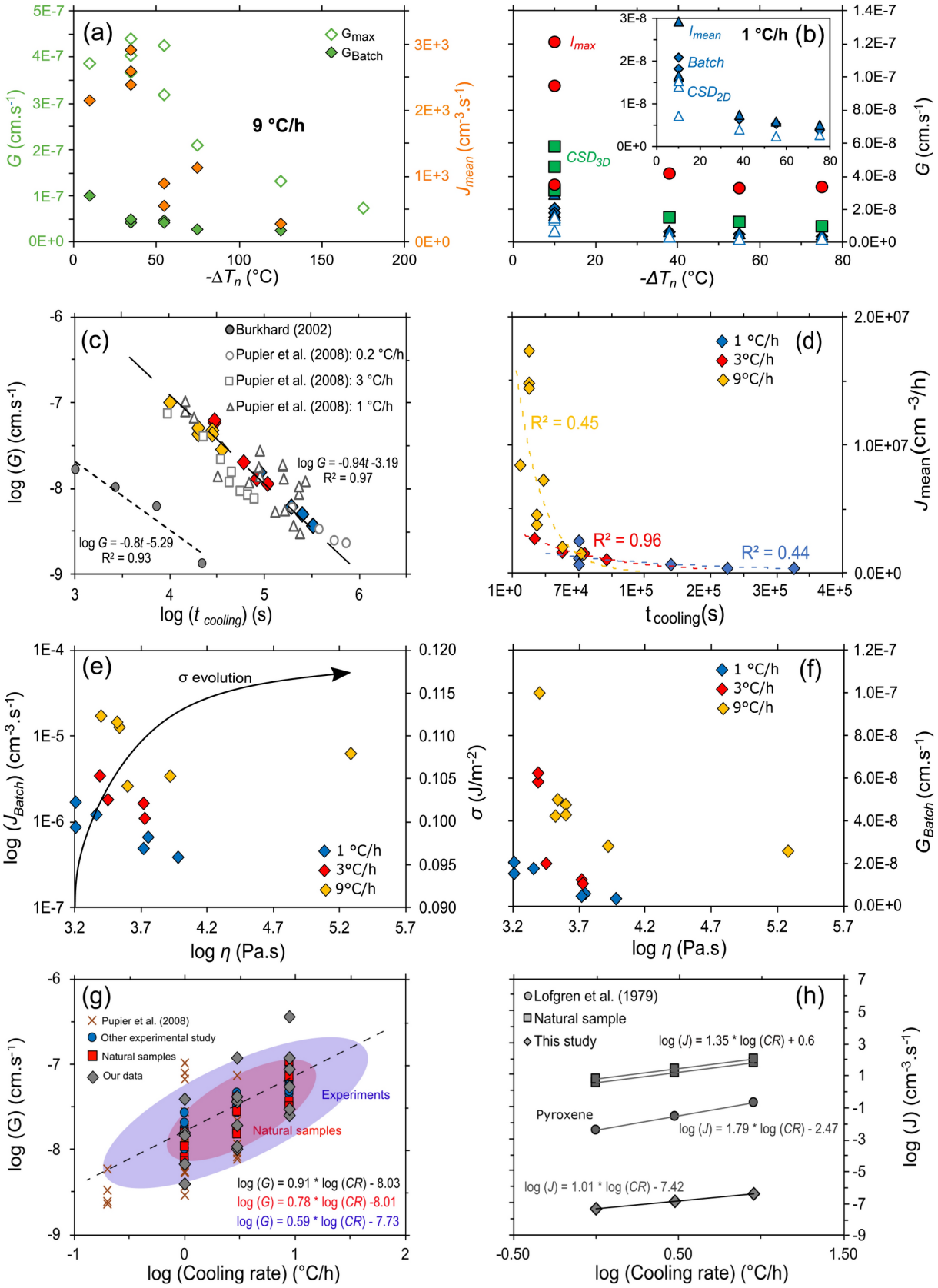
(a)
9 °C/h
G_{max}
G_{Batch}
G (cm.s^{-1})
J_{mean} (cm^{-3}.s^{-1})
-ΔT$_n$ (°C)
(b)
1 °C/h
I_{max}
I_{mean}
Batch
CSD_{2D}
CSD_{3D}
G (cm.s^{-1})
-ΔT$_n$ (°C)
(c)
Burkhard (2002)
Pupier et al. (2008): 0.2 °C/h
Pupier et al. (2008): 3 °C/h
Pupier et al. (2008): 1 °C/h
log G = -0.94t -3.19
R² = 0.97
log G = -0.8t -5.29
R² = 0.93
log (G) (cm.s^{-1})
log (t cooling) (s)
(d)
1 °C/h
3°C/h
9°C/h
R² = 0.45
R² = 0.96
R² = 0.44
J_{mean} (cm^{-3}/h)
t cooling(s)
(e)
σ evolution
1 °C/h
3°C/h
9°C/h
log (J_{Batch}) (cm^{-3}.s^{-1})
σ (J/m^{-2})
log η (Pa.s)
(f)
1 °C/h
3°C/h
9°C/h
G_{Batch} (cm.s^{-1})
log η (Pa.s)
(g)
Pupier et al. (2008)
Other experimental study
Natural samples
Our data
Experiments
Natural samples
log (G) = 0.91 * log (CR) - 8.03
log (G) = 0.78 * log (CR) -8.01
log (G) = 0.59 * log (CR) - 7.73
log (G) (cm.s^{-1})
log (Cooling rate) (°C/h)
(h)
Lofgren et al. (1979)
Natural sample
This study
log (J) = 1.35 * log (CR) + 0.6
Pyroxene
log (J) = 1.79 * log (CR) - 2.47
log (J) = 1.01 * log (CR) - 7.42
log (J) (cm^{-3}.s^{-1})
log (Cooling rate) (°C/h)

Fig. 6 Nucleation and growth rates determined from the cooling experiments. **a** The evolution of nucleation (J_{mean}, averaged from J_{batch}, $J_{CSD,3D}$, and $J_{CSD,2D}$) and growth rates (G_{batch} and $G_{max,l}$) in samples cooled at 9 °C/h. **b** G calculated by various methods ($G_{max,l}$, $G_{CSD,3D}$, $G_{CSD,2D}$, $G_{mean,l}$, and G_{batch}) for experiments cooled at 1 °C/h (G-1). **c** log (G) vs. log($t_{cooling}$); values from Pupier et al. (2008) and Burkhard (2002) concerning cooling and re-heating experiments on basaltic compositions are provided for comparison. **d** J_{mean} vs. cooling time. **e**, **f** J_{batch} and G_{batch}, respectively, vs. melt viscosity. The interfacial free energy (σ; calculated following Arzilli et al. 2015) is also indicated in (**e**). **g**, **h** G (obtained by l_{max}, Batch, l_{mean} and CSD methods) and J (obtained by Batch and CSD methods), respectively, vs. cooling rate. Except for data from Pupier et al. (2008), other experimental and natural data are from Cashman's (1993) compilation

shape variations observed in 2D sections, combined with sectioning effects, make it difficult to verify the transition from tabular/prismatic to compact crystals.

At advanced stages of crystallization (1050 °C and 1000 °C, $-\Delta T_n$ = 125–175 °C) and under fast cooling (9 °C/h), the absence of crystals smaller than 10 µm could result from suppressed nucleation and the dominance of growth because Ostwald ripening, a relatively slow process, is precluded at high degrees of undercooling (Cabane et al. 2005). Another explanation proposed by Marsh (1998) is the scarcity of the available liquid around 50% crystallinity that could induce a strong decrease of the nucleation.

Increased cooling rates also affect clinopyroxene and Fe–Ti oxides, which develop skeletal textures rather than the euhedral shapes observed at slower cooling rates (1 and 3 °C/h). Clinopyroxene crystallization is particularly dependent on the cooling rate, with nucleation delayed by 60 °C (marked by crystallization mediated by plagioclase) under a fast cooling rate of 9 °C/h. In contrast, no delay was observed for Fe–Ti oxides or plagioclase. The textural differences observed during crystallization (corresponding to $-\Delta T_n$) and between the various cooling rates correspond to an increase of the true degree of undercooling ($-\Delta T$), demonstrating the complexity of making direct comparisons. Furthermore, despite a significant increase in cooling rate from 1 to 9 °C/h, similar to values used by Pupier et al. (2008) on synthetic basalt, the resulting textural variations observed herein remain generally small compared to those observed studies conducted at very fast cooling rates exceeding 100–900 °C/h (Kohut and Nielsen 2004; Arzilli et al. 2019).

Determination of activation energies for nucleation and growth

We used the following equations to constrain the T dependence of J and G, as well as the activation energies of nucleation and growth (E_J and E_G, respectively; Burkhard 2005):

$$\ln(G) = \ln(G_0) - \frac{E_G}{RT} \quad (12)$$

$$\ln(J) = \ln(J_0) - \frac{E_J}{RT} \quad (13)$$

For the different methods of calculation used herein (e.g. batch, CSD), the average values of E_J and E_G are 280–424 and 128–443 kJ/mol, respectively, in agreement with those determined in the isothermal crystallization experiments of Burkhard (2005; around 300–350 kJ/mol). We observed a strong decrease (by more than 100 kJ/mol) when the cooling rate increases from 1 to 9 °C/h because increased cooling rates, and hence the degree of undercooling, favors crystal nucleation and growth. Indeed, crystallization time decreases as the cooling rate increases. Nucleation and growth rates are respectively more than 7 and 11 times faster during a cooling at 1 °C/h than 9 °C/h. Lesher et al. (1999) demonstrated that the solidification of a MORB basalt occurs 50 times faster in a magma cooled at 1000 °C/h than in one cooled at 10 °C/h. Similar E_J and E_G values are respectively observed between cooling at 3 and 9 °C/h, and between 1 and 3 °C/h.

Evolution of growth and nucleation rates during crystallization

Here, we focus our discussion on the evolution of growth and nucleation rates as a function of effective undercooling (which varies with temperature), as well as the true instantaneous degree of undercooling, which increases with increasing cooling rate. Because it is impossible to precisely determine the true instantaneous degree of undercooling, this discussion is necessarily qualitative.

Growth as a function of crystal axis

Marsh (1998) assumed that the log-linear part of a CSD in a closed system results from an exponential increase of nucleation at a constant growth rate, without modification over time or with crystal size. However, several lines of evidence show that this assumption is incorrect. Pupier et al. (2008) and Mangler et al. (2023) observed that as crystal size increases, crystal shape evolves from equant/prismatic (S/I = 0.7–0.8 for the smallest crystals, < 5–10 µm) to more bladed/tabular (S/I = 0.2–0.3 for crystals of 30–50 µm) (Fig. 5b; Supplementary file 4). Furthermore, they observed that stable shapes are only attained once crystals reach 50 µm in size, marked by only slight variations of S/I from 0.1 to 0.2.

Our results obtained with G_{mean}, G_{max} (faster along the l axis than along the w axis), and G_{CSD} ($G_{CSD,3D} = 2.8 \times G_{CSD,2D}$;

$R^2 = 0.94$) indicate that growth depends not only on crystal size, but also on crystal axis, with significant growth occurring along the 3D intermediate axis (2D major axis). The correlation between the aspect ratio and crystal size, as well as the curved shape of the CSDs (with a flattened trend toward larger crystals), suggests a growth rate dependent on crystal size (Eberl et al. 2002; Kyle and Eberl 2003), in contrast to the conclusions of Zieg and Lofgren (2006).

Some authors, such as Pupier et al. (2008) and Nie et al. (2014), suggested that the downturn of the CSD at the smallest crystal sizes could be explained by late-stage maturation processes, such as Ostwald ripening (characterized by the preferential dissolution of smaller crystals in favor of the growth of larger ones) or crystal agglomeration (synneusis). Although agglomeration textures with crystal clusters are present, no evidence of coalescence has been observed. Moreover, because our grain size measurements separated the various crystals of the clusters for individual measurements, clustering cannot explain the flattening and kinked portions of the CSDs observed for the largest and smallest size ranges, respectively. Similarly, except for experiments quenched at 1050 and 1000 °C, in which the proportion of the smallest crystals (< 10 µm) decreases sharply (Supplementary file 4), Ostwald ripening cannot explain this phenomenon in the other experiments, where this proportion remains nearly constant. In our case, as suggested by Cashman and Marsh (1988), resolution limits and sectioning effects, both of which reduce the probability of intersecting the smallest crystals, seem to better explain the obtained CSDs.

The role of temperature and cooling time

Nucleation and growth rates were calculated based on the duration of cooling below the liquidus (1175 °C). Because nuclei are likely formed at various steps during cooling, these rates represent minimum values. We obtained a linear correlation between log (J)/log (G) and log(t), with R^2 respectively of 0.88 and 0.90 (Fig. 6c; Supplementary file 5). The slope of the log(G)-log(t) plot (−0.94) is somewhat steeper than the range of −0.5 to −0.8 suggested for mafic systems by Grove (1978) and Kohut and Nielsen (2004). However, data from Pupier et al. (2008) are consistent with our results, with variations potentially due to the initial superliquidus pre-treatment. Variation of the nucleation rate near the liquidus induced a lower R^2 value in the log(J)-log(t) plot. The sharp decrease in nucleation rates at relatively small to moderate $-\Delta T_n$ (between 1165 and 1140 °C, depending on the cooling rate) indicates that nucleation slowed altogether shortly after cooling began (Fig. 6d). This evolution is consistent with the intercepts in our CSDs, which were stable between 1140 and 1100 °C (from −12.24 to −12.64 at 1 °C/h, and from −12.64 to −12.18 at 3 °C/h in the 2D CSDs; Supplementary file 4), before the strong decrease in the proportion of small plagioclase (< 10 µm) from 0.36 at 1100 °C to 0.01 at 1000 °C (Supplementary file 4). This sharp decrease could be due to (1) a potential decrease in the proportion of liquid and available space (Špillar and Dolejš 2014) or, more likely, (2) textural maturation suppressing further nucleation due to overgrowths on pre-existing crystals being energetically favorable. The absence of a systematic decrease in the CSD intercepts between 1140 and 1100 °C could be due to the nature of the initial material (synthetic powder vs. natural powder with pre-existing crystals), which, in our case might favor nucleation due to the initial presence of seeds. The high curvatures at the smallest crystal sizes due to heterogeneous nucleation may also have impacted the determined intercepts.

As for the nucleation rate, growth rate (G) decreased with increasing $-\Delta T_n$. The constant plagioclase sizes below 1100 °C in experiments cooled at 9 °C/h indicate a probable shutdown of growth at $-\Delta T_n > 100$ °C. In comparison, a recent in situ study of progressive olivine crystallization (Welsch et al. 2023) also indicated a non-constant growth rate characterized by a first stage of accelerating growth followed by growth at a constant rate and a final stage of slowing growth. Our measured plagioclase growth rates are likely the sum of these three stages, and thus 'bulk' growth rates. The observed decrease of nucleation and growth with time contradicts Marsh's (1988) assumption that nucleation rates increase exponentially at a constant growth rate (increasing ln(n_0), but a constant slope during cooling).

The exponential decrease of J and G (Supplementary file 5) with increasing run duration is correlated with a gradual increase in melt viscosity, from 1.62×10^3 Pa.s at 1165 °C to 9.55×10^3 Pa.s at 1100 °C. At an advanced crystallization stage, viscosity becomes significantly higher, reaching 10^5 Pa.s at 1050 °C and 10^7 Pa.s at 1000 °C (Supplementary file 5). This increase probably causes a slower Ca-Al diffusion at lower temperatures (Fig. 6e, f; Giordano et al. 2008). We used the Eyring equation to quantify the "network diffusivity" reflecting chemical transport at the crystal-melt interface (Mangler et al. 2023):

$$D = \frac{k_B \times T}{\lambda \times \eta} \tag{14}$$

where k_B is the Boltzman constant (J/K), T the final temperature (K), λ the diffusing element's diameter (0.14 nm for O^{2-}; Watkins et al. 2009; Mangler et al. 2023) and η the melt viscosity (Pa.s). As expected, Eyring diffusivity decreases as melt viscosity increases (Supplementary file 5), dropping from 10^{-14} m^2 s between 1165 and 1100 °C, to 10^{-16}–10^{-18} m^2 s at 1050 and 1000 °C. Except at 1050–1000 °C, where

values are 3–4 orders of magnitude lower than those of Mangler et al. (2023), values calculated between 1165 and 1100 °C under "dry" conditions are between those obtained in basalt and hydrous haplodacite.

The resulting J and G decrease is modest at slow cooling rates but more substantial at faster cooling rates (Pupier et al. 2008). Therefore, at the very slow cooling rates occurring in natural magma bodies, growth rates are likely to be nearly constant over time, as deduced by Marsh (1998) from natural data.

The impact of cooling rate

Plagioclase sizes, nucleation and growth rates are linearly correlated with cooling rate (Fig. 6g, h; l_c evolution with cooling rate in Supplementary file 4), consistent with previous observations (Walker et al. 1978; Cashman 1993; Pupier et al. 2008). The linear correlation between $\log(l_{max,avg})$ and log(CR) (CR being the cooling rate) is clearly temperature-dependent, with some fluctuations ($R^2 = 0.88$–0.99) probably due to the similarity of the cooling rates used herein (1–9 °C/h) compared to the wider range explored in other studies (1–9000 °C/h; Iezzi et al. 2008; Vetere et al. 2015; Giuliani et al. 2020). Indeed, we observed a slight decrease in the characteristic crystal size ($l_c = -1/\text{slope}$) with increasing cooling rate (Supplementary file 4).

The correlations between log(J) and log(G) with log(CR) are given by (for further details, see Supplementary file 5):undefined

$$log(J_{mean}) = (-6.43 \pm 0.19) + [(1.25 \pm 0.22) \times log(\frac{dT}{dt})]; R^2 > 0.9 \quad (15)$$

$$log(G) = (-8.029 \pm 0.360) + [(0.914 \pm 0.074) \times log(\frac{dT}{dt})]; R^2 > 0.9 \quad (16)$$

The slope of the linear correlation obtained for the growth rates (the average value of the different methods of calculation) falls barely within the 1σ error range of values summarized by Cashman (1993) from experimental and natural samples (slopes of 0.42–0.88); e note relative differences of 12–29% and 3–6% for slope and intercept values, respectively. As observed by Pupier et al. (2008), when considering each cooling rate series separately, trends in the J vs. $t_{cooling}$ plot are nearly linear (and even becomes rapidly "constant" at 1 °C/h) and broadly overlap at slow cooling rates (1, 3 °C/h). However, they become exponential, with fluctuations, at higher cooling rates (here, 9 °C/h) (Fig. 6d). This exponential decrease in J_{mean} (averaged from J_{batch}, $J_{CSD,2D}$, and $J_{CSD,3D}$) at slow cooling rates is explained by the system evolving toward equilibrium over time, resulting in decreasing nucleation and growth rates that approach zero as the true degree of undercooling nears zero.

For the experimental series cooled at 1 and 3 °C/h, the range of J and G values remains within the same order of magnitude as the cooling rate variations (Supplementary file 5). This fact, previously mentioned by Pupier et al. (2008) for cooling rates between 0.2 and 3 °C/h, is less visible in experiments cooled at 9 °C/h, in which some skeletal textures were observed. This suggests a near-thermodynamic equilibrium in the proportion of plagioclase, which remained consistent across each cooling rate.

Comparison of calculated growth and nucleation rates

Determining crystallization kinetics is a complex problem (Zieg and Marsh 2002) and the various methods used to quantify crystallization (e.g. here, batch, CSD, l_{mean}, l_{max}) tend to return different parameter values. In this section, we compare the results obtained using each method in an effort to determine which methods give the best results. No discussion will be presented here regarding the various assumptions concerning the CSD method (see next section for this).

We obtained nucleation rates by the two methods generally used: the batch method (J_{batch}), referring to an average value estimated by point counting (N_V; Eq. 2), and the CSD method ($J_{CSD,2D}$ and $J_{CSD,3D}$; Eq. 9), linking the intercept and growth rate estimated from the same data. Although the results of these methods are well correlated ($R^2 > 0.88$), strong variations are present (Supplementary file 5). Indeed, nucleation rates obtained by the batch method were 50–85% higher than those estimated from the 3D CSD, as observed by Brugger and Hammer (2010a), but quite close to those estimated with from the 2D CSD ($J_{CSD,2D} = (0.94 \pm 0.13) \times J_{batch}$ for the series cooled at 1 and 3 °C/h). The greatest variations occurred near the liquidus (heterogeneous nucleation, few crystals), and for the series cooled at 9 °C/h ($J_{CSD,2D} = (1.43 \pm 0.52) \times J_{batch}$), in which the microtextures were more variable. Uncertainties on J_{batch} result mainly from the impact of the image resolution of the smallest analyzable crystals (< 5 µm) and from coarsening and agglomeration processes. In contrast, J_{CSD} depends mainly on the slope (G) and intercept of the log-linear part of the CSD, parameters that are strongly dependent on the selected bin width (Supplementary file 4; Higgins 2000) and on the interpretation of the CSD shape. $J_{CSD,2D}$ values were 56–87% higher than $J_{CSD,3D}$ values, which account for sectioning effects. Because J and G are directly linked, a relative difference of 10–50% on the slope (Supplementary file 4) will certainly impact the determined value of J.

We similarly employed various common methods to determine growth rates, including the batch (G_{batch}), CSD (G_{CSD}), and l_{max} ($G_{max,l}$) methods, as well as additional methods focused exclusively on the overgrowths around seed crystals (G_{rim}; Shea and Hammer 2013) and on the average size of the entire segmented plagioclase population segmented ($G_{mean,l}$). Growth rates obtained using these methods differed by 1–2 orders of magnitude (Supplementary file 5).

G_{batch}, $G_{CSD,2D}$, and $G_{mean,l}$ values were very well correlated ($R^2 > 0.95$), returning values of the same order of magnitude (less than factor of 2 difference; Supplementary file 5). The differences are directly linked to the various estimations of the characteristic sizes (S_N, l_c, and l_{mean}; Supplementary file 4): $l_c = 0.61 \times S_N$, $R^2 = 0.95$; $l_{mean} = 1.31 \times S_N$, $R^2 = 0.99$. In the batch method, S_N depends only on crystal counts, with no consideration of axis and size variability among crystals, whereas l_{mean} corresponds to the average length of the l axis across the entire crystal population. Distinctly, l_c is directly obtained by linear regression of the CSDs and is subject to uncertainties, such as the number of crystals per size range, the interpreted boundaries of the steepest part of the curve, and the selected bin width.

$G_{max,l}$ (based on the 10 largest crystals) and $G_{CSD,3D}$ (measured on the 3D major axis L) gave the fasted growth rates. $G_{max,l}$, corresponding to the first crystals nucleated, was 2–15 times higher than the mean values estimated using $G_{batch}/G_{mean,1}$ or $G_{CSD,2D}$, consistent with estimates of Pupier et al. (2008) at similar cooling rates. Because of the presence of seeds in the cores of some of the largest crystals, $G_{max,l}$ tends to overestimate the growth rate. Accordingly, considering only the overgrowths (G_{rim}) returned values closer to those estimated from G_{batch} and $G_{mean,l}$: G_{rim} values were 1.6 ± 0.32 and 1.3 ± 0.25 times higher than G_{batch} and $G_{mean,l}$, respectively.

Because G_{mean} and G_{CSD} are both based on the entire segmented crystal population, they probably give a better estimation of the mean growth rate. As for the l_{mean} method, the CSD method is the most time consuming, but can link the nucleation/growth parameters with the experimental conditions to provide additional qualitative information such as the type of nucleation and the temporal evolution of crystal abundance per size range. Because of the size- and axis-dependence of growth rates, a combination of the CSD method ($G_{CSD,2D}$ and $G_{CSD,3D}$, providing mean G values along l and L, respectively) with the l_{max} method (providing a maximum growth rate) would constrain the possible range of growth rates. Importantly, Brugger and Hammer (2010b) and Cooper and Kent (2014) noted that order of magnitude of growth rate variation is directly reflected in determined magmatic timescales. However, these variations appear to result more from the duration of cooling/decompression (a factor of 8 difference between the series cooled at 1 and 9 °C/h) than from the calculation method.

Discussion on the theory of CSD for experimental conditions

Despite the similar log-linear CSD plots between batch crystallization models and steady-state open systems (see theory in Supplementary file 1), the CSD slope in a non-steady batch system, with continuous crystallization, depends on both nucleation and growth rates (Cashman and Marsh 1988; Marsh 1988, 1998). In the case of a closed (batch) system, CSD theory generally assumes an exponential increase in the nucleation rate at a constant growth rate (independent of time and crystal size). However, as also noted by Pupier et al. (2008) and Ni et al. (2014), several observations contradict this assumption. First, the non-permanent increase in the intercept value; stable between 1140 and 1100 °C (and with a significant decrease at 1050 and 1000 °C, when crystallinity reaches around 40–50%) do not support the hypothesis of an exponential increase in nucleation rate during the entire crystallization period. Second, the size-dependent crystal shape and the complex CSD curves observable after 1140 °C, characterized by a more flattened portion for the largest crystals (especially apparent at advanced stages of crystallization), highlight a size and time dependent crystal growth rate.

Moreover, since the crystal population in a closed system is never renewed, according to the theory established by Marsh (1998, 1998), except during the earliest stages of crystallization, the total crystallization time can only be estimated using the growth rates of the largest crystals (G_{max} in our case). As proposed by Pupier et al. (2008), the quantitative determination of nucleation (J) and growth (G) rates via CSD in a closed system (such as experimental samples) should be limited to the early stages of crystallization (between 1175 and 1165 °C in our case). During this period, CSD are effectively marked by an exponential increase total crystallinity remains below 5%, and the behavior of batch and open systems is comparable.

The role of experimental conditions on growth rates

We compared our determined growth rates with available literature data. We selected 20 experimental datasets, compiling > 400 growth rate estimates (Supplementary Material 6). Selected studies cover a range of experimental parameters, including the type of experiments (static or dynamic, with an additional shear rate), the nature of the initial material (synthetic vs. natural samples), the composition of the starting material (especially SiO_2 and H_2O contents), the crystallization path (initial degree of superheating, cooling/

decompression rate, the inclusion of a final isothermal step), and the method used to calculate G (l_{max}, batch, CSD). Experiments were performed under hydrous or anhydrous conditions, and crystallization was induced by decompression, cooling, or isothermally below the liquidus. The starting compositions range from basalt to rhyodacite; most studies were performed on basaltic compositions, with only a few on more evolved compositions such as andesite and dacite (e.g. Conte et al. 2006; Shea and Hammer 2013).

The nominal degree of undercooling ($-\Delta T_n$) does not account for the various rates of cooling/decompression and is therefore neither directly comparable with the true ($-\Delta T$) nor the effective degree of undercooling ($-\Delta T_{eff}$, caused by the change of the liquidus temperature due to degassing during decompression), the latter used in some decompression experiments under hydrous conditions (Hammer and Rutherford 2002; Mollard et al. 2012). We thus analyzed the growth rate variations as a function of the cooling/decompression time ($t_{cooling/decompression}$) or the cooling rate.

In Fig. 7a, growth rates calculated using different methods (l_{max}, batch, CSD) are plotted as a function of experimental duration. Our data plot within the range of other ex situ experimental data (10^{-11}–10^{-6} cm s^{-1}) obtained on 2D sections. In all datasets, G decreases with increasing time and -ΔT_n. These results are usually lower than growth rates obtained with in situ analyses (10^{-4}–10^{-3} cm s^{-1}; Arzilli et al. 2019; Le Gall et al. 2021), in which the beginning of nucleation and the end of growth are better constrained. Except for one set of points (Mollard et al. 2012), whose higher values may be due to the method of calculation, the method used does not seem have a large impact. Growth rates appear to be dependent on the cooling and decompression rates. Although it is difficult to directly compare the two, growth rate values (10^{-10}–10^{-5} cm s^{-1}) obtained in decompression experiments are similar to those obtained from cooling experiments (10^{-9}–10^{-6} cm s^{-1}), except at very high decompression rates. Recent studies by Vona and Romano (2013), and Vetere et al. (2021, 2024) focusing on dynamic isothermal experiments have shown the impact of strain rates on crystallization, with growth rates ranging from 10^{-8} to 10^{-6} cm s^{-1}. These values, which are from 1 to 2 orders of magnitude higher than those reported in other static studies such as Orlando et al. (2008) (10^{-9}–10^{-8} cm s^{-1}; Fig. 7a, Supplementary Material 6) under similar isothermal conditions and comparable growth rate determination methods, can be explained by more efficient transport near the liquid–crystal interface. Our growth rate values, ranging between 10^{-9} and 10^{-7} cm s^{-1} in cooling experiments, confirm the lowest values obtained under "static" conditions.

Our growth rates (10^{-9}–10^{-7} cm s^{-1}) are equivalent to those of Pupier al. (2008; 10^{-9}–10^{-8} cm s^{-1}) obtained under similar cooling conditions in a basaltic starting material. Comparison of rates determined for basalts (Agostini et al. 2013; Moschini et al. 2023) and dacites (Hammer and Rutherford 2002; Brugger and Hammer 2010a, b) in hydrous decompression experiments shows that the growth rates obtained for these distinct compositions partly overlap, with a trend towards lower G values in dacites (Fig. 7b). We note that data from Shea and Hammer (2013) for basaltic andesite overlap with results obtained using basaltic compositions, and are two orders of magnitude higher than those obtained using dacitic compositions (10^{-11}–10^{-9} cm s^{-1}; Hammer and Rutherford 2002; Couch et al. 2003b). The significantly higher values of Mollard et al. (2012), i.e. 3–5 orders of magnitude higher than those Hammer and Rutherford (2002) or Brugger and Hammer (2010a, b), likely result from decompression rates 15 to > 2000 times faster than those used by Brugger and Hammer (2010a, b), and perhaps their use of a crystal-free starting material. As mentioned by Brugger and Hammer (2010a), the cooling path strongly controls the growth rate (Fig. 7c) and can potentially hide the compositional influence.

Another potential important compositional parameter is H_2O, which substantially lowers melt viscosity. Comparison of our data on an anhydrous basaltic andesite with data from Shea and Hammer (2013) on a similar composition under hydrous conditions (Fig. 7d), as well as the few anhydrous data of Conte et al. (2006), demonstrates that plagioclase growth rates are less than an order of magnitude faster in hydrous conditions, perhaps because of the faster diffusion of plagioclase-forming elements in the liquid.

Conclusions

This study had three main objectives: (1) to examine the evolution of crystal size, density, and shape textural parameters during the slow cooling (< 10 °C/h) of an anhydrous basaltic andesite; (2) to determine plagioclase nucleation (J) and growth rates (G) for those experiments; and (3) to compare the various methods of calculating J and G, with the goal of determining the most appropriate method for deriving timescales from textural analyses of natural samples. Our results and their implications are as follows:

During cooling, plagioclase crystal shape (2D aspect ratio) varied significantly, evolving from blocky and equant/elongate to tabular/bladed. Crystal sizes and number densities followed the same overall trend: increasing as cooling progressed down to $-\Delta T_n = 80$ °C, then decreasing at the most advanced stages of crystallization.

Crystal sizes and phase proportions were independent of the cooling rate. However, increased cooling rates favor

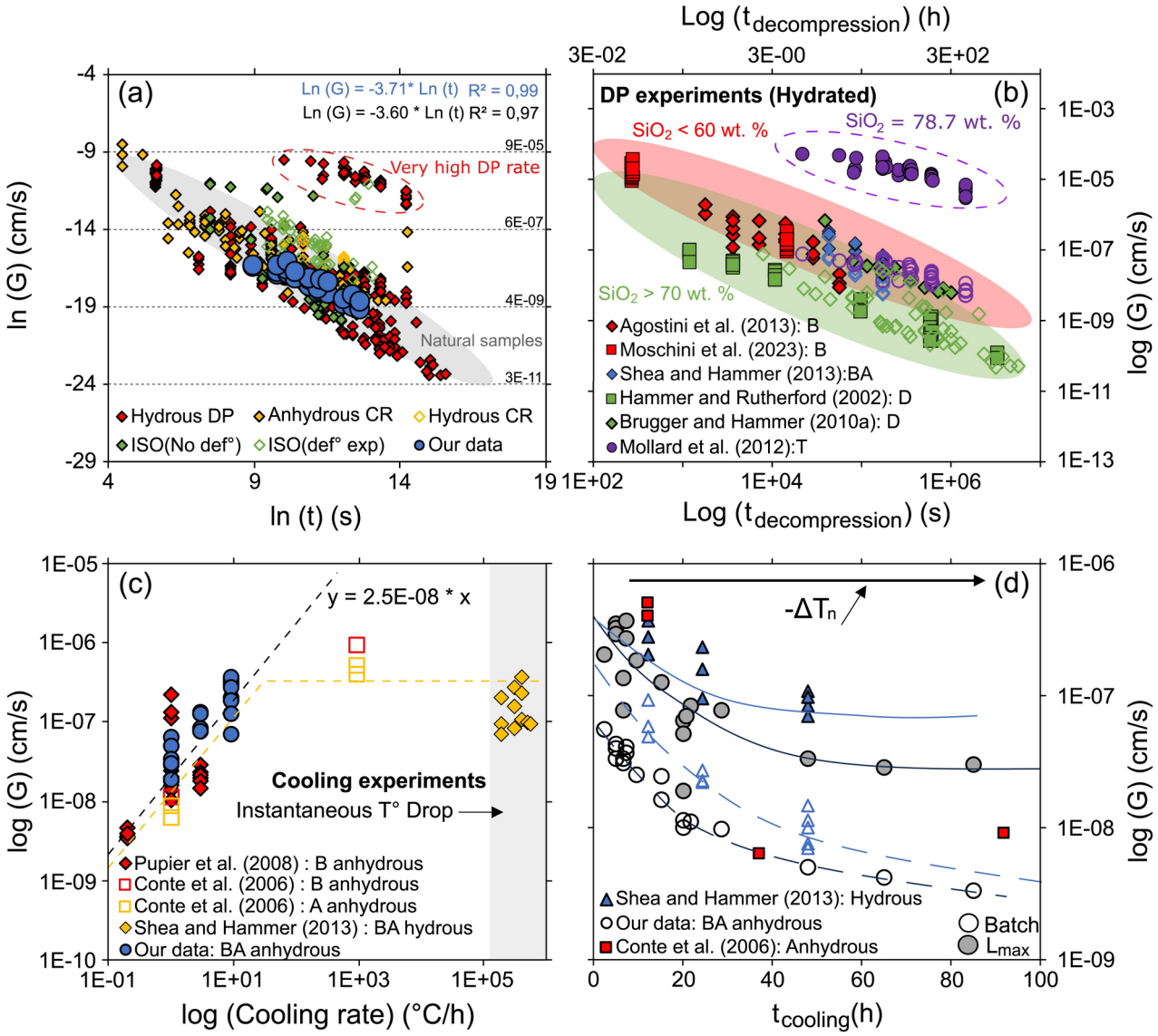

Fig. 7 Comparison of our plagioclase growth rates with published data. Twenty studies (list provided in Supplementary Material 5) using different experimental setups (initial composition, water content, cooling/decompression path, final dwell time, etc.) were selected, comprising >400 growth rates. *DP* decompression experiments, *CR* cooling rate experiments, *ISO* isothermal experiments, *B* basalt, *BA* basaltic andesite, *A* andesite, *D* dacite, *T* tonalite. **a** Global comparison between our results and literature experimental data without discrimination of the crystallization path. Isothermal experiments are separated in two groups, corresponding to "static" experiments (without shear rate), and "dynamic" experiments with a shear rate. The gray field corresponds to natural samples (Cashman 1993). The data are generally grouped with some scatter. **b** Hydrous decompression experiments performed using starting compositions ranging from basalt to dacite, highlighting a decrease of G with increasing SiO_2 content and experimental duration. Open and filled symbols denote results calculated using the batch and l_{max} methods, respectively. **c** Cooling experiments on basalt and basaltic andesite starting compositions as a function of cooling rate. All experiments are anhydrous, except those of Shea and Hammer (2013). Conte et al. (2006) used an instantaneous temperature drop. Our data fill a lack of data for basaltic andesite compositions. **d** log(G) vs. cooling time in experiments using intermediate compositions (basaltic andesite, andesite) as starting materials (open symbols, G_{batch}; filled symbols, $G_{max,l}$). The growth rates estimated by Shea and Hammer (2013) in hydrous conditions are slightly higher than ours obtained in anhydrous conditions. Logarithmic scales are used to facilitate comparison and to clarify the diagrams

increased crystal number densities and the formation of elongate crystals with skeletal/dendritic habits.

Nucleation and growth rates similarly increased to a maximum at 1165 °C ($-\Delta T_n$ = 15 °C: 1 and 3 °C/h) or 1140 °C ($-\Delta T_n$ = 40 °C: 9 °C/h), before decreasing at more advanced stages of crystallization.

J and G increased by an order of magnitude with increasing cooling rate from 1 to 9 °C/h. This increase was correlated with cooling time and was minimal at slower cooling

rates (1 and 3 °C/h) where J and G remained nearly constant over time, but became exponential at 9 °C/h.

- Our growth rates (between 2.04×10^{-9} and 4.39×10^{-7} cm s^{-1}) overlap with those of Pupier et al. (2008), measured at similar cooling conditions in a basaltic composition, and of Shea and Hammer (2013), acquired under instantaneous cooling conditions in a hydrous basaltic andesite.
- Comparison of the different methods to calculate G (l_{max}, batch, $l_{mean}G_{CSD,2D}$, $G_{CSD,3D}$) indicates that differences in experimental conditions lead to greater variability than the method of calculation. G_{batch} is the least time-consuming method but provides the least accurate values. In contrast, G_{mean} and G_{CSD} both based on the entire segmented crystal population, give better estimations of the mean growth rate. Although the CSD method requires the selection of certain parameters (e.g., bin width, and shape model), it gives the most accurate average estimations, whether considering 2D or 3D long axes. Because growth rates are size-dependent, coupling this method with the l_{max} method can constrain the full range of possible rates.

Our comparison with other experimental datasets indicated that plagioclase growth rates depend more on the thermal history and initial treatment of the starting material than on the composition of the starting material. This complicates the application of CSDs for the determination of the timescales of magmatic processes such as ascent rate and storage time. Furthermore, as discussed above, except during the earliest stages of crystallization, the various assumptions underlying the closed-system CSD (as for Cashman and Marsh 1988; Pupier et al. 2008; and Brugger and Hammer 2010b) theory do not appear to hold true. Therefore, the quantitative determination of J and G should be conducted with caution, particularly in the case of experimental samples.

Declaration

Conflict of interest

Not applicable.

Supplementary Information The online version contains supplementary material available at https://doi.org/10.1007/s00410-025-02213-9.

Acknowledgements We thank Roman Klinghardt for his help during the SEM and EPMA analyses (RWTH Aachen, Germany) as well as Tonin Bechon and Yishen Zhang for facilitating EPMA calibration and measurements at LMV (Clermont-Ferrand, France) and KU Leuven (Belgium). We thank Robert Dennen from RD Geoscience Editing for his help during the preparation of the manuscript. We also thank Martin Mangler and Michel Pichavant, as well as the two other reviewers, for their constructive comments, which helped us improve the quality of the paper.

Author contributions Project Conceptualization: Billon Melvyn, Charlier Bernard, Namur Olivier, Vander Auwera Jacqueline; Methodology: Billon Melvyn, Charlier Bernard; Material preparation and realization of the experiments: Billon Melvyn; Analyses and interpretation: Billon Melvyn; Discussion: All authors the first draft of the manuscript was written by Billon Melvyn and all authors commented on previous versions of the manuscript. All authors read and approved the final manuscript.

Funding This work was partly funded by the FNRS PDR grant T.0079.18 to JVDA. BC is a Research Associate of the Belgian Fund for Scientific Research-FNRS. MB acknowledges support from a FRIA-FNRS fellowship (Fonds pour la Formation à la Recherche dans l'Industrie et dans l'Agriculture—Fonds de la Recherche Scientifique) (Grant FC 41073).

Data availability Supplementary data are available as supplementary electronic files, and also in Zenodo repository at https://doi.org/10.5281/zenodo.15013047 but are subject to embargo until publication. All supplementary data for the review are labelled as *Supplementary data/file for the website.*

References

Agostini C, Fortunati A, Arzilli F, Landi P, Carroll MR (2013) Kinetics of crystal evolution as a probe to magmatism at Stromboli (Aeolian Archipelago, Italy). Geochim Cosmochim Acta 110:135–151. https://doi.org/10.1016/j.gca.2013.02.027

Armienti P (2008) Decryption of igneous rock textures: crystal size distribution tools. Rev Mineral Geochem 69:623–649. https://doi.org/10.2138/rmg.2008.69.16

Armienti P, Pareschi MT, Innocenti F, Pompilio M (1994) Effects of magma storage and ascent on the kinetics of crystal growth: the case of the 1991–93 Mt. Etna eruption. Contrib Miner Petrol 115:402–414. https://doi.org/10.1007/BF00320974

Armienti P, Perinelli C, Putirka KD (2013) A new model to estimate deep-level magma ascent rates, with applications to Mt. Etna (Sicily, Italy). J Petrol 54:795–813. https://doi.org/10.1093/petrology/egs085

Arzilli F, Mancini L, Voltolini M, Cicconi MR, Mohammadi S, Giuli G, Mainprice D, Paris E, Barou F, Carroll MC (2015) Near-liquidus growth of feldspar spherulites in trachytic melts: 3D morphologies and implications in crystallization mechanisms. Lithos 216–217:93–105. https://doi.org/10.1016/j.lithos.2014.12.003

Arzilli F, La Spina G, Burton MR, Polacci M, Le Gall N, Hartley ME, Di Genova D, Cai B, Vo NT, Bamber EC, Nonni S, Atwood R, Llewellin EW, Brooker RA, Mader HM, Lee PD (2019) Magma fragmentation in highly explosive basaltic eruptions induced by rapid crystallization. Nat Geosci 12:1023–1028. https://doi.org/10.1038/s41561-019-0468-6

Bechon T, Billon M, Namur O, Bolle O, Fugmann P, Foucart H, Devidal J-L, Delmelle N, Vander Auwera J (2022) Petrology of the magmatic system beneath Osorno volcano (Central Southern Volcanic Zone, Chile). Lithos 426–427:106777. https://doi.org/10.1016/j.lithos.2022.106777

Bennett EN, Lissenberg CJ, Cashman KV (2019) The significance of plagioclase textures in mid-ocean ridge basalt (Gakkel Ridge, Arctic Ocean). Contrib Miner Petrol 174:49. https://doi.org/10.1007/s00410-019-1587-1

Berkebile CA, Dowty E (1982) Nucleation in laboratory charges of basaltic composition. Am Miner 67:886–899

Brugger CR, Hammer JE (2010a) Crystal size distribution analysis of plagioclase in experimentally decompressed hydrous rhyodacite magma. Earth Planet Sci Lett 300:246–254. https://doi.org/10.1016/j.epsl.2010.09.046

Brugger CR, Hammer JE (2010b) Crystallization kinetics in continuous decompression experiments: implications for interpreting natural magma ascent processes. J Petrol 51:1941–1965. https://doi.org/10.1093/petrology/egq044

Burkhard DJ (2002) Kinetics of crystallization: example of microcrystallization in basalt lava. Contrib Miner Petrol 142:724–737. https://doi.org/10.1007/s00410-001-0321-x

Burkhard DJ (2005) Nucleation and growth rates of pyroxene, plagioclase, and Fe–Ti oxides in basalt under atmospheric conditions. Eur J Mineral 17:675–685. https://doi.org/10.1127/0935-1221/2005/0017-0675

Cabane H, Laporte D, Provost A (2005) An experimental study of Ostwald ripening of olivine and plagioclase in silicate melts: implications for the growth and size of crystals in magmas. Contrib Miner Petrol 150:37–53. https://doi.org/10.1007/s00410-005-0002-2

Cashman KV (1990) Chapter 10. Textural constrains on the kinetics of crystallization of igneous rocks. In: Nicholls J, Russel JK (eds) Modern methods of igneous petrology: understanding magmatic processes. De Gruyter, pp 259–314

Cashman KV (1993) Relationship between plagioclase crystallization and cooling rate in basaltic melts. Contrib Miner Petrol 113:126–142. https://doi.org/10.1007/BF00320836

Cashman KV, Marsh BD (1988) Crystal size distribution (CSD) in rocks and the kinetics and dynamics of crystallization II: Makaopuhi lava lake. Contrib Miner Petrol 99:292–305. https://doi.org/10.1007/BF00375363

Cassidy M, Castro JM, Helo C, Troll VR, Deegan FM, Muir D, Neave DA, Mueller SP (2016) Volatile dilution during magma injections and implications for volcano explosivity. Geology 44:1027–1030. https://doi.org/10.1130/G38411.1

Conte AM, Perinelli C, Trigila R (2006) Cooling kinetics experiments on different Stromboli lavas: Effects on crystal morphologies and phases composition. J Volcanol Geoth Res 155:179–200. https://doi.org/10.1016/j.jvolgeores.2006.03.025

Cooper K, Kent A (2014) Rapid remobilization of magmatic crystals kept in cold storage. Nature 506:480–483. https://doi.org/10.1038/nature12991

Corrigan GM (1982a) Supercooling and the crystallization of plagioclase, olivine, and clinopyroxene from basaltic magmas. Mineral Mag 46:31–42. https://doi.org/10.1180/minmag.1982.046.338.06

Corrigan GM (1982b) The crystal morphology of plagioclase feldspar produced during isothermal supercooling and constant rate cooling experiments. Mineral Mag 46:433–439. https://doi.org/10.1180/minmag.1982.046.341.04

Costa F, Dohmen R, Chakraborty S (2008) Time scales of magmatic processes from modeling the zoning patterns of crystals. Rev Mineral Geochem 69:545–594. https://doi.org/10.2138/rmg.2008.69.14

Couch S, Sparks RSJ, Carroll MR (2001) Mineral disequilibrium in lavas explained by convecting self-mixing in open magma chambers. Nature 411:1037–1039 https://doi.org/10.1038/35082540

Couch S, Harford CL, Sparks RSJ, Carroll MR (2003a) Experimental constraints on the conditions of formation of highly calcic plagioclase microlites at the Soufrière Hills Volcano, Montserrat. J Petrol 44:1455–1475. https://doi.org/10.1093/petrology/44.8.1455

Couch S, Sparks RSJ, Carroll MR (2003b) The kinetics of degassing-induced crystallization at Soufrière Hills Volcano, Montserrat. J Petrol 44:1477–1502. https://doi.org/10.1093/petrology/44.8.1477

Del Gaudio P, Mollo S, Ventura G, Iezzi G, Taddeucci J, Cavallo A (2010) Cooling rate-induced differentiation in anhydrous and hydrous basalts at 500 MPa: implications for the storage and transport of magmas in dikes. Chem Geol 270:164–178. https://doi.org/10.1016/j.chemgeo.2009.11.014

Delesse MA (1847) Procédé mécanique pour déterminer la composition des roches. Comptes Rendus De L'académie des Sci (Paris) 25:544–545

Eberl DD, Kile DE, Drits VA (2002) On geological interpretations of crystal size distributions: constant vs. proportionate growth. Am Miner 87:1235–1241. https://doi.org/10.2138/am-2002-8-923

Faure F, Tissandier L (2014) Contrasted liquid lines of descent revealed by olivine-hosted melt inclusions and the external magma. J Petrol 55:1779–1798. https://doi.org/10.1093/petrology/egu041

Faure F, Trolliard G, Nicollet C, Montel JM (2003) A developmental model of olivine morphology as a function of the cooling rate and the degree of undercooling. Contrib Miner Petrol 145:251–263. https://doi.org/10.1007/s00410-003-0449-y

Fokin VM, Zanotto ED, Yuritsyn NS, Schmelzer JWP (2006) Homogeneous crystal nucleation in silicate glasses: a 40 years perspective. J Non-Cryst Solids 352:2681–2714. https://doi.org/10.1016/j.jnoncrysol.2006.02.074

Gibb FGF (1974) Supercooling and the crystallization of plagioclase from a basaltic magma. Mineral Mag 39:641–653. https://doi.org/10.1180/minmag.1974.039.306.02

Giordano D, Russell JK, Dingwell DB (2008) Viscosity of magmatic liquids: a model. Earth Planet Sci Lett 271:123–134. https://doi.org/10.1016/j.epsl.2008.03.038

Giuliani L, Iezzi G, Vetere F, Behrens H, Mollo S, Cauti F, Ventura G, Scarlato P (2020) Evolution of textures, crystal size distributions and growth rates of plagioclase, clinopyroxene and spinel crystallized at variable cooling rates from a mid-ocean ridge basaltic melt. Earth Sci Rev 204:103165. https://doi.org/10.1016/j.earscirev.2020.103165

Griffiths TA, Habler G, Ageeva O, Sutter C, Ferrière L, Abart R (2023) The origin of lattice rotation during dendritic crystallization of clinopyroxene. J Petrol 64:1–19. https://doi.org/10.1093/petrology/egac125

Grove TL (1981) Use of FePt alloys to eliminate the iron loss problem in 1 atmosphere gas mixing experiments: theoretical and practical considerations. Contrib Miner Petrol 78:298–304. https://doi.org/10.1007/BF00398924

Grove TL, Baker MB (1984) Phase equilibrium controls on the tholeiitic versus calc-alkaline differentiation trends. J Geophys Res 89:3253–3274. https://doi.org/10.1029/JB089iB05p03253

Grove TL (1978) Cooling histories of Luna 24 very low Ti (VLT) Ferrobasalts: an experimental study. Lunar and Planetary Science Conference 9th, 565–584.

Gualda GAR, Ghiorso MS, Lemons RV, Carley TL (2012) Rhyolite-MELTS: a modified calibration of MELTS optimized for silica-rich, fluid-bearing magmatic systems. J Petrol 53:875–890. https://doi.org/10.1093/petrology/egr080

Hammer JE (2008) experimental studies of the kinetics and energetics of magma crystallization. Rev Mineral Geochem 69:9–59. https://doi.org/10.2138/rmg.2008.69.2

Hammer JE, Rutherford MJ (2002) An experimental study of the kinetics of decompression-induced crystallization in silicic melt. J Geophys Res. https://doi.org/10.1029/2001JB000281

Hammer JE, Cashman KV, Hoblitt RP, Newman S (1999) Degassing and microlite crystallization during pre-climactic events of the 1991 eruption of Mt. Pinatubo, Philippines. Bull Volcanol 60:355–380. https://doi.org/10.1007/s004450050238

Higgins MD (2000) Measurement of crystal size distributions. Am Miner 85:1105–1116. https://doi.org/10.2138/am-2000-8-901

Honour VC, Holness MB, Charlier B, Piazolo SC, Namur O, Prosa TJ, Martin I, Helz RT, Maclennan J, Jean MM (2019) Compositional boundary layers trigger liquid unmixing in a basaltic crystal mush. Nat Commun 10:4821. https://doi.org/10.1038/s41467-019-12694-5

Humphreys M, Menand T, Blundy JD, Klimm K (2008) Magma ascent rates in explosive eruptions: Constraints from H_2O diffusion in melt inclusions. Earth Planet Sci Lett 270:25–40. https://doi.org/10.1016/j.epsl.2008.02.041

Iezzi G, Mollo S, Ventura G, Cavallo A, Romano C (2008) Experimental solidification of anhydrous latitic and trachytic melts at different cooling rates: the role of nucleation kinetics. Chem Geol 253:91–101. https://doi.org/10.1016/j.chemgeo.2008.04.008

Kent AJR, Darr C, Koleszar AM, Salisbury MJ, Cooper KM (2010) Preferential eruption of andesitic magmas through recharge filtering. Nat Geosci 3:631–636. https://doi.org/10.1038/ngeo924

Kirkpatrick RJ (1975) Crystal growth from the melt: a review. Am Miner 60:798–814

Kirkpatrick RJ (1977) Nucleation and growth of plagioclase, Makaopuhi and Alae lava lakes, Kilauea Volcano. Hawaii Geol Soc Am Bull 88:78–84. https://doi.org/10.1130/0016-7606(1977)88%3c78:NAGOPM%3e2.0.CO;2

Kirkpatrick RJ (1981) Kinetics of crystallization of igneous rocks. Rev Mineral Geochem 8:321–398

Kohut E, Nielsen RL (2004) Melt inclusion formation mechanisms and compositional effects in high-an feldspar and high-Fo olivine in anhydrous mafic silicate liquids. Contrib Miner Petrol 147:684–704. https://doi.org/10.1007/s00410-004-0576-0

Kyle DE, Eberl DD (2003) On the origin of size-dependent and size-independent crystal growth: influence of advection and diffusion. Am Miner 88:1514–1521. https://doi.org/10.2138/am-2003-1014

Le Gall N, Arzilli F, La Spina G, Polacci M, Cai B, Hartley ME, Vo NT, Atwood RC, Di Genova D, Nonni S, Llewellin EW, Burton MR, Lee PD (2021) In situ quantification of crystallisation kinetics of plagioclase and clinopyroxene in basaltic magma: implications for lava flow. Earth Planet Sci Lett 568:117016. https://doi.org/10.1016/j.epsl.2021.117016

Lesher CE, Cashman KV, Mayfield JD (1999) Kinetic controls on crystallization of tertiary North Atlantic basalt and implications for the emplacement and cooling history of lava at site 989, Southeast Greenland rifted margin. Proc Ocean Drill Program 163:138–145

Lofgren GE (1974) An experimental study of plagioclase crystal morphology: isothermal crystallization. Am J Sci 274:243–273

Lofgren GE (1983) Effect of heterogeneous nucleation on basaltic textures: a dynamic crystallization study. J Petrol 24:229–255. https://doi.org/10.1093/petrology/24.3.229

Mangler MF, Humphreys MCS, Wadsworth FB, Iveson AA, Higgins MD (2022) Variation of plagioclase shape with size in intermediate magmas: a window into incipient plagioclase crystallisation. Contrib Miner Petrol 177:64. https://doi.org/10.1007/s00410-022-01922-9

Mangler MF, Humphreys MCS, Geifman E, Iveson AA, Wadsworth FB, Brooker RA, Lindoo A, Hammond K (2023) Melt diffusion-moderated crystal growth and its effect on euhedral crystal shapes. J Petrol. https://doi.org/10.1093/petrology/egad054

Marsh BD (1988) Crystal size distribution (CSD) in rocks and the kinetics and dynamics of crystallization. I Theory J Petrol 99:277–291

Marsh BD (1998) On the interpretation of crystal size distributions in magmatic systems. J Petrol 39:553–599. https://doi.org/10.1093/petroj/39.4.553

Mollard E, Martel C, Bourdier JL (2012) Decompression-induced crystallization in hydrated silica-rich melts: empirical models of experimental plagioclase nucleation and growth kinetics. J Petrol 53:1743–1766. https://doi.org/10.1093/petrology/egs031

Mollo S, Misiti V, Scarlato P, Soligo M (2012) The role of cooling rate in the origin of high temperature phases at the chilled margin of magmatic intrusions. Chem Geol 322–323:28–46. https://doi.org/10.1016/j.chemgeo.2012.05.029

Morgado E, Parada MA, Contreras C, Castruccio A, Gutiérrez F, McGee LE (2015) Contrasting records from mantle to surface of Holocene lavas of two nearby arc volcanic complexes: Caburgua-Huelemolle small eruptive centers and Villarrica Volcano, Southern Chile. J Volcanol Geoth Res 306:1–16. https://doi.org/10.1016/j.jvolgeores.2015.09.023

Morse SA (2013) Experimental equilibrium tested by plagioclase loop widths. J Petrol 54:1793–1813. https://doi.org/10.1093/petrology/egt031

Moschini P, Mollo S, Pontesilli A, Nazzari M, Petrone CM, Fanara S, Vona A, Gaeta M, Romano C, Scarlato P (2023) A review of plagioclase growth rate and compositional evolution in mafic alkaline magmas: guidelines for thermometry, hygrometry, and timescales of magma dynamics at Stromboli and Mt. Etna Earth-Sci Rev 240:104399. https://doi.org/10.1016/j.earscirev.2023.104399

Nabelek PI, Taylor LA, Lofgren GE (1978) Nucleation and growth of plagioclase and the development of textures in a high-alumina basaltic melt. Lunar Planetary Science Conference 9th, 725–741.

Ni H, Keppler H, Walte N, Schiavi F, Chen Y, Masotta M, Li Z (2014) In situ observation of crystal growth in a basalt melt and the development of crystal size distribution in igneous rocks. Contrib Miner Petrol 167:1003. https://doi.org/10.1007/s00410-014-1003-9

Orlando AD, Armienti P, Borrini D (2008) Experimental determination of plagioclase and clinopyroxene crystal growth rates in an anhydrous trachybasalt from Mt Etna (Italy). Eur J Mineral 20:653–664. https://doi.org/10.1127/0935-1221/2008/0020-1841

Pichavant M, Costa F, Burgisser A, Scaillet B, Martel C, Poussineau S (2007) Equilibration scales in silicic to intermediate magmas implications for experimental studies. J Petrol 48:1955–1972. https://doi.org/10.1093/petrology/egm045

Pupier E, Duchene S, Toplis MJ (2008) Experimental quantification of plagioclase crystal size distribution during cooling of a basaltic liquid. Contrib Miner Petrol 155:555–570. https://doi.org/10.1007/s00410-007-0258-9

Reubi O, Blundy J (2009) A dearth of intermediate melts at subduction zone volcanoes and the petrogenesis of arc andesites. Nature 461:1269–1273. https://doi.org/10.1038/nature08510

Rusiecka MK, Bilodeau M, Baker DR (2020) Quantification of nucleation delay in magmatic systems: experimental and theoretical approach. Contrib Miner Petrol 175:47. https://doi.org/10.1007/s00410-020-01682-4

Rutherford MJ (2008) Magma ascent rates. Rev Mineral Geochem 69:241–271. https://doi.org/10.2138/rmg.2008.69.7

Sato H (1995) Textural difference between pahoehoe and aa lavas of Izu-Oshima volcano, Japan—an experimental study on population density of plagioclase. J Volcanol Geoth Res 66:101–113. https://doi.org/10.1016/0377-0273(94)00055-L

Schiavi F, Walte N, Keppler H (2009) First in situ observation of crystallization processes in a basaltic-andesitic melt with the moissanite cell. Geology 37:963–966. https://doi.org/10.1130/G30087A.1

Shea T, Hammer JE (2013) Kinetics of cooling- and decompression-induced crystallization in hydrous mafic-intermediate magmas. J Volcanol Geoth Res 260:127–145. https://doi.org/10.1016/j.jvolgeores.2013.04.018

Špillar V, Dolejš D (2014) Kinetic model of nucleation and growth in silicate melts: implications for igneous textures and their

quantitative description. Geochim Cosmochim Acta 131:164–183. https://doi.org/10.1016/j.gca.2014.01.022

Špillar V, Dolejš D (2015) Heterogeneous nucleation as the predominant mode of crystallization in natural magmas: numerical model and implications for crystal–melt interaction. Contrib Miner Petrol 169:4. https://doi.org/10.1007/s00410-014-1103-6

Sunagawa I (1977) Natural crystallization. J Cryst Growth 45:3–12. https://doi.org/10.1016/0022-0248(77)90197-X

Sunagawa I (1981) Characteristics of crystal growth in nature as seen from the morphology of mineral crystals. Bull De Mineral 104:2–3. https://doi.org/10.3406/bulmi.1981.7438

Toplis MJ, Carroll MR (1995) An experimental study of the influence of oxygen fugacity on Fe–Ti oxide stability, phase relations, and mineral-melt equilibria in ferro-basaltic systems. J Petrol 36:1137–1170. https://doi.org/10.1093/petrology/36.5.1137

Vander Auwera J, Namur O, Dutrieux A, Wilkinson CM, Ganerod M, Coumont V, Bolle O (2019) Mantle melting and magmatic processes under la picada stratovolcano (CSVZ, Chile). J Petrol 60:907–944. https://doi.org/10.1093/petrology/egz020

Vetere F, Iezzi G, Behrens H, Holtz F, Ventura G, Misiti V, Cavallo A, Mollo S, Dietrich M (2015) Glass forming ability and crystallisation behaviour of sub-alkaline silicate melts. Earth Sci Rev 150:25–44. https://doi.org/10.1016/j.earscirev.2015.07.001

Vetere F, Petrelli M, Perugini D, Haselbach S, Morgavi D, Pisello A, Iezzi G, Holtz F (2021) Rheological evolution of eruptible Basaltic-Andesite Magmas under dynamic conditions: the importance of plagioclase growth rates. J Volcanol Geoth Res 420:107411. https://doi.org/10.1016/j.jvolgeores.2021.107411

Vetere F, Merseburger S, Pisello A, Perugini D, Viti C, Petrelli M, Musu A, Almeev R, Caricchi L, Iezzi G, Cassetta M, Holtz F (2024) The role of deformation on the early crystallization and rheology of basaltic liquids. Earth Planet Sci Lett 644:118934. https://doi.org/10.1016/j.epsl.2024.118934

Vona A, Romano C (2013) The effects of undercooling and deformation rates on the crystallization kinetics of Stromboli and Etna basalts. Contribut Mineral Petrol 166:491–509. https://doi.org/10.1007/s00410-013-0887-0

Walker D, Powell MA, Lofgren GE, Hays JF (1978) Dynamic crystallization of a eucrite basalt. Proc. Lunar Planetary Science Conference 9th, 1369–1391.

Watkins JM, DePaolo DJ, Huber C, Ryerson FJ (2009) Liquid composition-dependence of calcium isotope fractionation during diffusion in molten silicates. Geochim Cosmochim Acta 73(24):7341–7359. https://doi.org/10.1016/j.gca.2009.09.004

Watson EB (1996) Surface enrichment and trace-element uptake during crystal growth. Geochim Cosmochim Acta 60:5013–5020. https://doi.org/10.1016/S0016-7037(96)00299-2

Watson EB, Liang Y (1995) A simple model for sector zoning in slowly grown crystals: implications for growth rate and lattice diffusion, with emphasis on accessory minerals in crustal rocks. Am Miner 80:1179–1187. https://doi.org/10.2138/am-1995-11-1209

Welsch B, Faure F, First EC (2023) Reappraising crystallization kinetics with overgrowth chronometry: an in situ study of olivine growth velocities. J Petrol. https://doi.org/10.1093/petrology/egad055

Zieg MJ, Lofgren GE (2006) An experimental investigation of texture evolution during continuous cooling. J Volcanol Geoth Res 154:74–88. https://doi.org/10.1016/j.jvolgeores.2005.09.020

Zieg MJ, Marsh BD (2002) Crystal size distributions and scaling laws in the quantification of igneous textures. J Petrol 43:85–101. https://doi.org/10.1093/petrology/43.1.85

Zingg T (1935) Beitrag zur schotteranalyse. Schweiz Mineral Petrogr Mitt 15:39–140